

See discussions, stats, and author profiles for this publication at: <https://www.researchgate.net/publication/261740344>

Anodes for Sodium Ion Batteries Based on Tin-Germanium-Antimony Alloys

ARTICLE in ACS NANO · APRIL 2014

Impact Factor: 12.88 · DOI: 10.1021/nn4063598 · Source: PubMed

CITATIONS

52

READS

211

10 AUTHORS, INCLUDING:



Kai Cui

National Research Council Canada

22 PUBLICATIONS 553 CITATIONS

SEE PROFILE



M.R. Kupsta

National Research Council Canada

21 PUBLICATIONS 230 CITATIONS

SEE PROFILE



Benjamin Zehri

University of Alberta

24 PUBLICATIONS 647 CITATIONS

SEE PROFILE



Elmira Memarzadeh

University of Alberta

20 PUBLICATIONS 454 CITATIONS

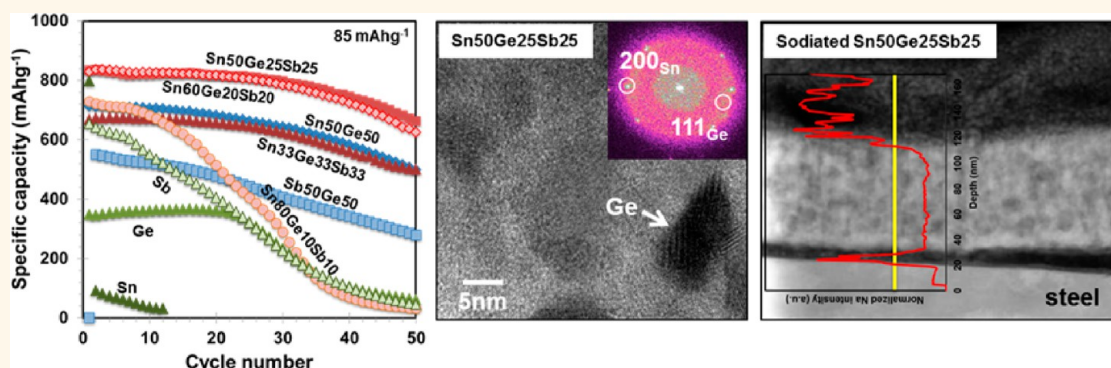
SEE PROFILE

Anodes for Sodium Ion Batteries Based on Tin–Germanium–Antimony Alloys

Behdokht Farbod,^{†,*} Kai Cui,[‡] W. Peter Kalisvaart,^{†,*} Martin Kupsta,[‡] Benjamin Zahiri,^{†,*} Alireza Kohandehghan,^{†,*} Elmira Memarzadeh Lotfabad,^{†,*} Zhi Li,^{†,*} Erik J. Lubner,^{§,5} and David Mitlin^{†,*}

[†]Department of Chemical and Materials Engineering, University of Alberta, 9107 116th Street, Edmonton, Alberta, T6G 2V4, Canada, [‡]National Institute for Nanotechnology (NINT), NRC, 11421 Saskatchewan Drive, Edmonton, Alberta, T6G 2M9, Canada, and [§]Department of Chemistry, University of Alberta, Edmonton, Alberta, T6G 2G2, Canada,

ABSTRACT



Here we provide the first report on several compositions of ternary Sn–Ge–Sb thin film alloys for application as sodium ion battery (aka NIB, NaB or SIB) anodes, employing Sn50Ge50, Sb50Ge50, and pure Sn, Ge, Sb as baselines. Sn33Ge33Sb33, Sn50Ge25Sb25, Sn60Ge20Sb20, and Sn50Ge50 all demonstrate promising electrochemical behavior, with Sn50Ge25Sb25 being the best overall. This alloy has an initial reversible specific capacity of 833 mAhg^{−1} (at 85 mAhg^{−1}) and 662 mAhg^{−1} after 50 charge–discharge cycles. Sn50Ge25Sb25 also shows excellent rate capability, displaying a stable capacity of 381 mAhg^{−1} at a current density of 8500 mAhg^{−1} (~10C). A survey of published literature indicates that 833 mAhg^{−1} is among the highest reversible capacities reported for a Sn-based NIB anode, while 381 mAhg^{−1} represents the optimum fast charge value. HRTEM shows that Sn50Ge25Sb25 is a composite of 10–15 nm Sn and Sn-alloyed Ge nanocrystallites that are densely dispersed within an amorphous matrix. Comparing the microstructures of alloys where the capacity significantly exceeds the rule of mixtures prediction to those where it does not leads us to hypothesize that this new phenomenon originates from the Ge(Sn) that is able to sodiate beyond the 1:1 Na:Ge ratio reported for the pure element. Combined TOF-SIMS, EELS TEM, and FIB analysis demonstrates substantial Na segregation within the film near the current collector interface that is present as early as the second discharge, followed by cycling-induced delamination from the current collector.

KEYWORDS: sodium ion battery · NIB · NaB · SIB · lithium ion battery · LIB · anode · Sn · Sb · Ge · thin film

While lithium ion batteries (LIBs) are the dominant secondary energy storage source for portable and electric vehicle applications, there are some concerns about lithium's cost and continued availability. Sodium ion batteries (NIBs) have recently attracted much scientific attention as alternatives to LIBs, since sodium is more readily available than lithium and has a potential for significant associated cost reduction.^{1–6} Moreover NIBs are considered as the key technology for meeting large-scale energy storage needs,^{7–9} mainly

due to much more “geographically democratic” availability of Na and lower cost as compared to Li. NIBs also offer an increased resistance to metal plating-induced shorts.¹⁰ The standard electrode potential is determined by the redox couple and by the ion solvation interactions, with the difference between Li and Na standard potentials in carbonate solvents being in the range 0.2–0.25 V.¹¹ Several classes of cathode materials have been proposed for NIBs, including Na_{0.44}MnO₂, Na_{0.85}Li_{0.17}Ni_{0.21}Mn_{0.64}O₂, Na_{0.7}CoO₂, Na₃V₂(PO₄)₂F₃, Na₂FePO₄F,

* Address correspondence to pkalisvaart@gmail.com, dmitlin@ualberta.ca.

Received for review December 11, 2013 and accepted March 26, 2014.

Published online March 26, 2014
10.1021/nn4063598

Published 2014 by the American Chemical Society

LiFeSO₄F, and Na_{4-α}M_{2+α/2}(P₂O₇)₂ ($2/3 \leq \alpha \leq 7/8$, M = Fe, Fe_{0.5}Mn_{0.5}, Mn), olivines, and NASICONs.^{2,12,13} NIB anodes, on the other hand, present more of a challenge since commercial graphite has very low Na storage capacity.¹⁴ Charge storage capacities and cycling stabilities approaching LIB graphite have been demonstrated for various amorphous or partially graphitic carbons.^{15–20} Anodes based on titanium oxide, such as Na₂Ti₃O₇ and anatase TiO₂, have also been successfully employed. These are highly desirable from a cost and environmental friendliness perspective, while offering capacities of ~ 150 mAh g⁻¹ and good cycling stability.^{21–27} These materials along with the carbons represent perhaps the most economical anode option for large-scale stationary applications.

As in the case of Li, other group 14 elements besides carbon have potentially higher storage capacities for sodium.²⁸ According to the equilibrium phase diagram, Sn can store 3.75 Na/host-atom (Na_{1.5}Sn₄),²⁹ with a resulting maximum charge storage capacity of 847 mAhg⁻¹. The experimentally measured capacity of Sn anodes generally approach this value early in testing, but degrades during cycling.^{5,8,30–33} For instance, Yamamoto *et al.*³⁰ reported a NIB negative electrode based on a Sn thin film with a discharge (charge) capacity of 790 (729) mAhg⁻¹ in the first cycle. However, this electrode showed a rapid capacity decay after 15 cycles. Ellis *et al.*³⁴ also observed an initial discharge capacity of ~ 850 mAhg⁻¹ for a sputtered Sn electrode and a rapid cycling-induced capacity degradation to near zero. Sn-based alloy composites have been reported to exhibit improved cycling stability, such as (Sn_{0.5}Co_{0.5})_{1-x}C_x alloy,³⁴ (Cu₆Sn₅)_{1-x}C_x,³⁵ SnSb/C nanocomposite,⁴ Cu₆Sn₅,³⁶ Sn_{0.9}Cu_{0.1} alloy,³⁷ and Sn–SnS–C nanocomposite.³⁸

Antimony has also been recently examined for its potential as a NIB anode.^{39–42} The maximum stoichiometry of Na–Sb alloys is Na₃Sb,^{29,43} giving Sb a theoretical capacity of 660 mAhg⁻¹. Authors have examined Sb alloy and intermetallic electrodes, including Cu₂Sb with a capacity of 280 mAhg⁻¹,⁴⁴ AlSb with a capacity of 490 mAhg⁻¹,⁴⁵ Mo₃Sb₇ with a capacity of 330 mAhg⁻¹,⁴⁶ and Sb-MWCNT nanocomposites with a capacity of ~ 500 mAhg⁻¹.⁴⁷ Germanium in thin film form or as porous nanocolumnar structures has been demonstrated to work as a NIB anode as well.^{48,49} Experimental capacities in the range 1:1 NaGe (369 mAhg⁻¹) have been reported.

While binary and several ternary (containing C) Sn- and Sb-based alloys have been examined as potential NIB anodes, little is known regarding Ge-containing systems. Here we provide the first report on thin film-based ternary Sn–Ge–Sb alloy anodes. In order to better understand the role of each element in determining the electrochemical properties of the ternary system and to obtain baselines for clear comparisons, elemental Ge, Sb, and Sn and binary Sn–Ge and Sb–Ge

alloys are also evaluated. Our results demonstrate a highly promising reversible capacity and rate capability in Sn₆₀Ge₂₀Sb₂₀ and Sn₅₀Ge₂₅Sb₂₅ alloys. These findings should serve as a useful guide for designing improved formulations of NIB electrode materials in bulk, using methods such as powder co-mechanical milling and rapid solidification.

RESULTS AND DISCUSSION

TEM images of the as-deposited 100 nm thick elemental films are shown in Figure S3. The as-deposited Sn, as shown in Figure S3a–c, is composed of relatively large crystallites of various orientations. The as-sputtered pure Ge (Figure S3d,e) is diffraction amorphous (*i.e.*, amorphous, nanocrystalline, or a combination of the two), as evidenced by the washed-out selected area diffraction (SAD) ring pattern. The as-deposited Sb film is continuous and polycrystalline, with the grain size being large enough to generate single-crystal SAD patterns when the smallest field-limiting aperture is employed (Figure S3f–h). The crystallinity of pure Sn and Sb and the amorphous/nanocrystalline structure of Ge are confirmed by XRD analysis, as shown in Figure S4. These results are in good agreement with previous studies on Sn, Ge, and Sb films.^{38,40,48,51}

Figure 1a,b show TEM micrographs and the indexed SAD pattern of the as-synthesized Sn₅₀Ge₅₀ alloy, which is a two-phase nanocomposite. Polycrystalline Sn is detected, as the (200), (101), and (211) Sn diffraction rings are visible in the SAD pattern. Two additional reflections belonging to Ge are also present. The associated *d*-spacings for the (111) and (220) Ge rings are expanded by $\sim 6\%$ with respect to elemental Ge, indicating that there is extended substitutional solid solubility of Sn in Ge, likely much beyond the equilibrium 1%. XRD analysis of the as-synthesized materials, shown in Figure S4, confirms this shift in the Ge lattice parameter. As is marked in the figure, the equilibrium position of the Ge (111) reflection (the film is highly textured) should be at $2\theta = 27.30^\circ$, whereas it is located at $2\theta = 25.70^\circ$, corresponding to a 6% shift in the lattice parameter, which is the same as measured by TEM. Figure 1c presents TEM analysis of the as-deposited Sb₅₀Ge₅₀. The equilibrium Sb–Ge phase diagram demonstrates negligible room-temperature solubility and no intermediate phases. However, as evidenced by the SAD pattern, co-sputtering of Sb and Ge results in the formation of an amorphous alloy with the broad rings corresponding to the first and the second nearest neighbors. This conclusion is also confirmed by the XRD pattern of this alloy shown in Figure S4. Figure 1d, e show the Sn₈₀Ge₁₀Sb₁₀ microstructure, which consists of nanocrystalline Sn with no evidence of Ge or Sb precipitates. TEM analysis of Sn₃₃Ge₃₃Sb₃₃ is presented in Figure 1f. Analysis of Sn₅₀Ge₂₅Sb₂₅ is shown in Figures 1g–i. The Sn₃₃Ge₃₃Sb₃₃ alloy

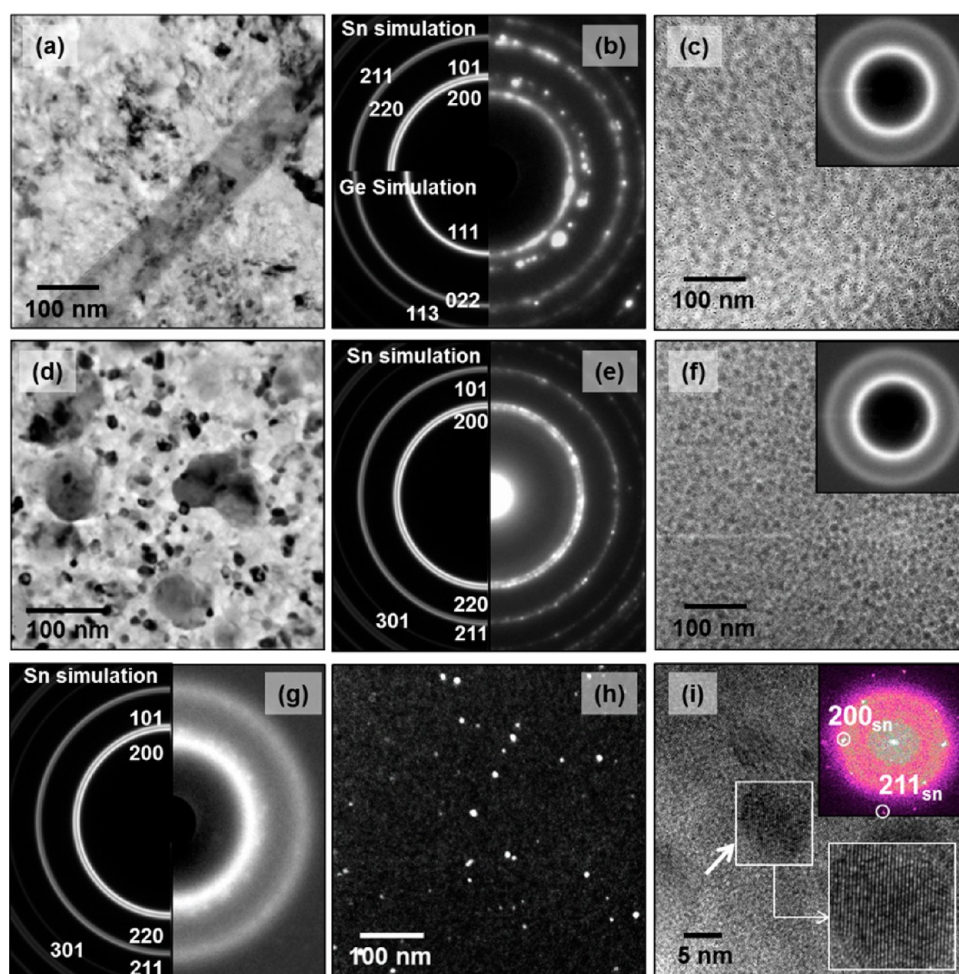


Figure 1. TEM analysis of as-synthesized alloys (pure Sn, Sb, Ge are shown in the SI): (a, b) Sn50Ge50, bright field micrograph and simulated SAD with the Sn-induced expansion of the Ge lattice being taken into account. (c) Sb50Ge50, (d and e) Sn80Ge10Sb10, (f) Sn33Ge33Sb33, and (g–i) Sn50Ge25Sb25. The dark field image (h) was taken using a portion of the (200) and (101) Sn rings. (i) HRTEM micrograph showing a Sn nanocrystallite (arrowed) embedded in an amorphous matrix. The corresponding FFT is shown in the inset.

appears amorphous, while Sn50Ge25Sb25 has a two-phase structure consisting of an amorphous phase and nanocrystalline Sn. The Sn nanocrystals may be imaged in dark field (Figure 1h) and by HRTEM (Figure 1i). The Sn-rich side of the ternary Sn–Ge–Sb diagram consists of a mixture of Sn, SbSn, and Ge phases with appreciable mutual solubility.⁵² However, we detected no crystalline phases besides Sn. This means the rest of the material will consist of an amorphous matrix that may be compositionally homogeneous or segregated.

The trend of larger amounts of the amorphous phase with greater GeSb content can be better understood by analyzing the glass-forming ability (GFA) of all three binary alloys, *i.e.*, GeSb, SnGe, and SnSb. From previous studies of co-sputtered films of GeSb,⁵³ SnGe,⁵⁴ and SnSb,⁵⁵ it is found that both GeSb and SnSb films deposited over a wide range of compositions possess an amorphous microstructure, while SnGe does not exhibit an amorphous phase at any of the studied compositions (also confirmed in our data). Moreover, the GFAs of GeSb⁵³ and SnSb⁵⁵ alloys are

found to be highest when both components are in roughly equal proportion (*i.e.*, ~50 at. % Sb). As such, we would expect to have the highest fraction of amorphous phase when both the Sn/Sb and Ge/Sb ratios are close to 1. For the films considered in this study the Ge/Sb ratio is always fixed at 1, while the Sn/Sb ratio approaches 1 as the GeSb content is increased relative to Sn. Specifically the condition of both Sn/Sb and Ge/Sb ratios being equal to 1 is satisfied at Sn33Ge33Sb33, which is found to consist completely of amorphous phase. However, it must be noted that this analysis is only a qualitative guide to understanding the trends that we observe; to more fully understand this phenomenon, it is necessary to characterize the GFA properties of the ternary Sn–Ge–Sb *via* calorimetric or diffraction heating experiments.

The sodiation behavior of the elemental films is shown in Figure S5. Pure Sn was tested at 85 mAg⁻¹, Ge was tested at 110 mAg⁻¹, while Sb was tested at 120 mAg⁻¹. For pure Sn the reversible capacity drops to 38 mAhg⁻¹ after only 10 cycles, far below its theoretical

value. This agrees with previous studies on sodiation of pure Sn, where the materials degrade very rapidly during cycling.^{30,31,34,56} During the first sodiation process, there are four sloping plateaus at roughly 0.45, 0.18, 0.08, and 0.03 V, although the only equilibrium phase that is observed to form electrochemically is $\text{Na}_{15}\text{Sn}_4$. Upon charging, the plateaus are at approximately 0.15, 0.28, 0.55, and 0.63 V. The plateaus become less distinct with cycling. The reversible capacity of Ge is 349 mAhg^{-1} , being close to a 1:1 ratio of Na/Ge (369 mAhg^{-1}) and agreeing with a previous report.⁴² The voltage profile of Ge presents an initial sharply sloping plateau during the first and subsequent sodiation cycles from $\sim 1 \text{ V}$ down to 0.1–0.15 V, followed by a flat plateau at 0.1–0.15 that remains until complete discharge. There is a large hysteresis in the charge/discharge behavior, with the flat desodiation plateau being at 0.6 V during charge. The reversible capacity of Sb is 650 mAhg^{-1} , which is close to the theoretical 660 mAhg^{-1} . In the pure Sb films, the voltage profiles show two sloping plateaus during sodiation, centered around 0.75 and 0.55 V. Only two stable intermetallics, NaSb and Na_3Sb , are known in the Na–Sb system.²⁹ Intermediate phases may be possible, as the voltage profile is not sharp enough to confirm or negate their presence. During desodiation two plateaus are observed at around 0.78 and 0.85 V. The voltage profiles along with the TEM analysis of the postcycled microstructure indicate that the desodiated Sb film is still crystalline after 10 cycles. Both elemental Ge and elemental Sb degrade during cycling, though not at a rate as fast as Sn. The sodiation voltage profiles of the individual elements are generally in agreement with previous reports.^{8,39,48,49}

Figure S6 shows the TEM analysis of the cycled elemental Sn, elemental Ge, and elemental Sb electrodes. All sodiated samples are characterized after the first Na insertion, while desodiated samples are characterized after five full cycles. Figure S6a–c show sodiated pure Sn, d–f show desodiated Sn, g–i show sodiated Ge, j, k show desodiated Ge, l–n show sodiated pure Sb, and o–q show desodiated Sb. The dark field image in Figure S6c is taken using a portion of the (022) and (013) $\text{Na}_{15}\text{Sn}_4$ diffraction rings. The dark field image in Figure S6f is taken from the $g = (200)_{\text{Sn}}$ diffraction spot. The formation of the $\text{Na}_{15}\text{Sn}_4$ terminal phase is confirmed by TEM characterization of the Sn electrode discharged to 0.01 V. Desodiation leads to the formation of crystalline Sn. This is consistent with previous *in situ* observations.^{32,57} These findings are confirmed by XRD analysis, as presented in Figure S7. For the as-synthesized specimen, the (111), (110), and (211) peaks are respectively located at $2\theta = 23.77^\circ$, 28.77° , and 40.13° . For the desodiated one, these are located at $2\theta = 23.83^\circ$, 28.89° , and 40.39° , indicating that the crystalline structure is restored without any noticeable changes in the lattice parameter. TEM

analysis indicates that the Ge electrode sodiated to 0.01 V is partially nanocrystalline, although the exact phase could not be identified. Similar to recent reports on Ge thin films,^{48,49} it seems that the sodiation process of Ge reaches a metastable phase that is not on the equilibrium Na–Ge phase diagram. The desodiated Ge sample is diffraction amorphous.

Figure 2 shows the voltage *versus* capacity behavior for the binary and the ternary alloys, which were tested at 85 mA g^{-1} . The constant current voltage profile of $\text{Sn}_{50}\text{Ge}_{50}$, shown in Figure 2a, reveals three sloping sodiation plateaus at approximately 0.28, 0.19, and 0.03 V. The system displays two sloping desodiation plateaus near 0.16 and 0.6 V. The voltage profiles, particularly for desodiation, are nearly identical for cycles 1–10, indicating a stable microstructure. For the second to tenth cycle, Coulombic efficiency (CE) is nearly 100%, with a reversible capacity of 713 mAhg^{-1} . This is substantially more than what is expected based on a weighted average (the alloy is Sn–38%Ge by weight) of theoretical capacities of the elemental films (665 mAhg^{-1}). The voltage profiles of $\text{Sb}_{50}\text{Ge}_{50}$ are shown in Figure 2b. The reversible capacity is 551 mAhg^{-1} , which is close to a rule of mixtures prediction (the alloy is Sb–37%Ge by weight) based on either the experimental or the theoretical values for Sb and Ge. The stable cycling voltage behavior of this alloy demonstrates a single broad monotonically decreasing slope between 0.8 and 0.2 V upon discharge and between 0.6 and 1.2 V upon charging. The absence of sharply defined plateaus indicates that there are no two-phase regions, with each phase being energetically distinct. Rather there is a continuing variation in occupational site energies, as would be expected for a solid solution with a continuously varying Na content or with nanocrystals where a second phase is difficult to nucleate due to size effects.

The constant current voltage profiles for the Sn–Ge–Sb alloys are presented in Figures 2c–f. At least three voltage plateaus, each with a distinct flat or sloping profile, are observed both upon charge and discharge in every alloy. Qualitatively, the voltage *vs* capacity profiles of the ternary systems are more similar to that of Sn–Ge than to Sb–Ge. Moreover the position and the slope of the plateaus evolve with alloy composition. The measured reversibly capacities of $\text{Sn}_{80}\text{Ge}_{10}\text{Sb}_{10}$, $\text{Sn}_{60}\text{Ge}_{20}\text{Sb}_{20}$, $\text{Sn}_{50}\text{Ge}_{25}\text{Sb}_{25}$, and $\text{Sn}_{33}\text{Ge}_{33}\text{Sb}_{33}$ are 728, 829, 833, and 669 mAhg^{-1} , respectively. This is an intriguing finding since the values for $\text{Sn}_{60}\text{Ge}_{20}\text{Sb}_{20}$ and $\text{Sn}_{50}\text{Ge}_{25}\text{Sb}_{25}$ are considerably above the weighted average of the elemental capacities. For instance one can assume the known theoretical capacity of Sn (847 mAhg^{-1}) and of Sb (660 mAhg^{-1}) and a 1:1 Na/Ge ratio (369 mAhg^{-1}). In that case alloys $\text{Sn}_{80}\text{Ge}_{10}\text{Sb}_{10}$ (Sn–6wt%Ge–10Sb), $\text{Sn}_{60}\text{Ge}_{20}\text{Sb}_{20}$ (Sn–13wt%Ge–22Sb), $\text{Sn}_{50}\text{Ge}_{25}\text{Sb}_{25}$ (Sn–17wt%Ge–28Sb), and $\text{Sn}_{33}\text{Ge}_{33}\text{Sb}_{33}$ (Sn–23wt%

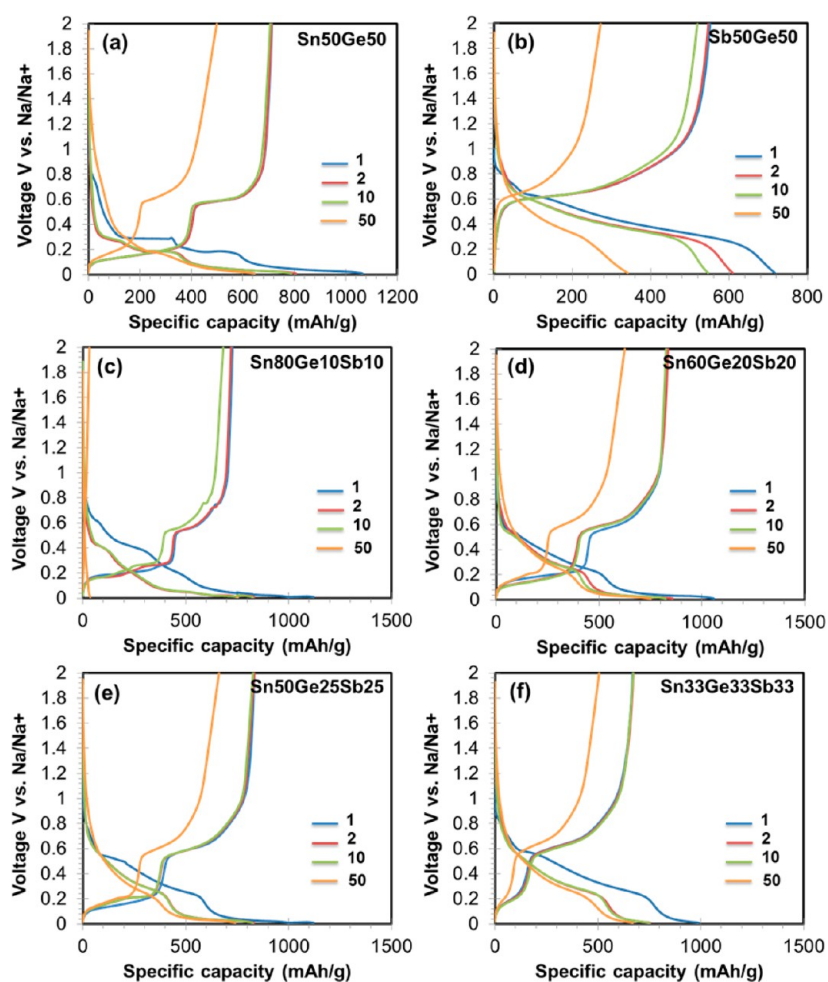


Figure 2. Constant current voltage profiles of binary and ternary alloys. All systems were tested at 85 mA g^{-1} .

Ge–39Sb) should be 800, 743, 714, and 664 mAh g^{-1} , respectively.

As the TEM micrographs in Figure 3a–c demonstrate, the cycled microstructure of Sn50Ge50 contains both Sn and Ge nanocrystallites. The dark field image in Figure 3c highlights the nanocrystalline nature of the cycled material. The Ge nanocrystals still contain solutionized Sn, with the Ge diffraction rings being closer than the equilibrium spacing (Sn would expand the Ge lattice). From the (111) reflection, the lattice constant is estimated as approximately 5.92 \AA , which is 4.77% larger than elemental Ge (5.65 \AA). From measurements of the nearest-neighbor distance in Ge–20at.%Sn films, 2.7 \AA ,⁵⁸ it can be inferred that Sn strongly expands the Ge lattice and that the amount of dissolved Sn in the Ge phase is at maximum 10 at.% or less. Figure S7 shows the XRD patterns of desodiated binary Sn–Ge and Sb–Ge and ternary Sn50Ge25Sb25 alloys. It is confirmed that Ge contains Sn in substitutional solid solution, with a comparable shift in the 2θ values of the (111) Ge XRD Bragg peaks. As is marked in the figure, the equilibrium position of the Ge (111) reflection (the film is highly textured) should be at $2\theta = 27.30^\circ$, whereas it is located at $2\theta = 26.04^\circ$, corresponding

to a 4.8% shift in the lattice parameter. The broad background intensity in the TEM SAD indicates that there is also substantial presence of an amorphous phase. This is reasonable as the initially fully amorphous alloy is expected to decompose relatively slowly at room temperature, especially concomitantly with the insertion/extraction of Na ions. As Figures 3d–f demonstrate, the desodiated Sb50Ge50 microstructure consists of a dense distribution of Ge nanocrystallites embedded in an amorphous matrix. For the case of Sb–Ge, the Ge crystallites, they have a lattice parameter at the equilibrium value, demonstrating negligible solutionizing of Sb. This is the key difference between the Sn–Ge and Sb–Ge, where in the latter case the Sb atoms are unable to remain in Ge substitutional solid solution during cycling, which leads us to conclude that that observed Ge lattice expansion in the Sn–Ge–Sb alloy is likewise due to the effect of Sn.

Figure 4a presents the SAD pattern of a steady-state microstructure of the desodiated Sn50Ge25Sb25 alloy after 10 cycles. Although the sample was X-ray amorphous (Figure S7b), it was possible to resolve the crystallites in the electron diffraction patterns. The desodiated Sn50Ge25Sb25 is a multiphase nanocomposite. According

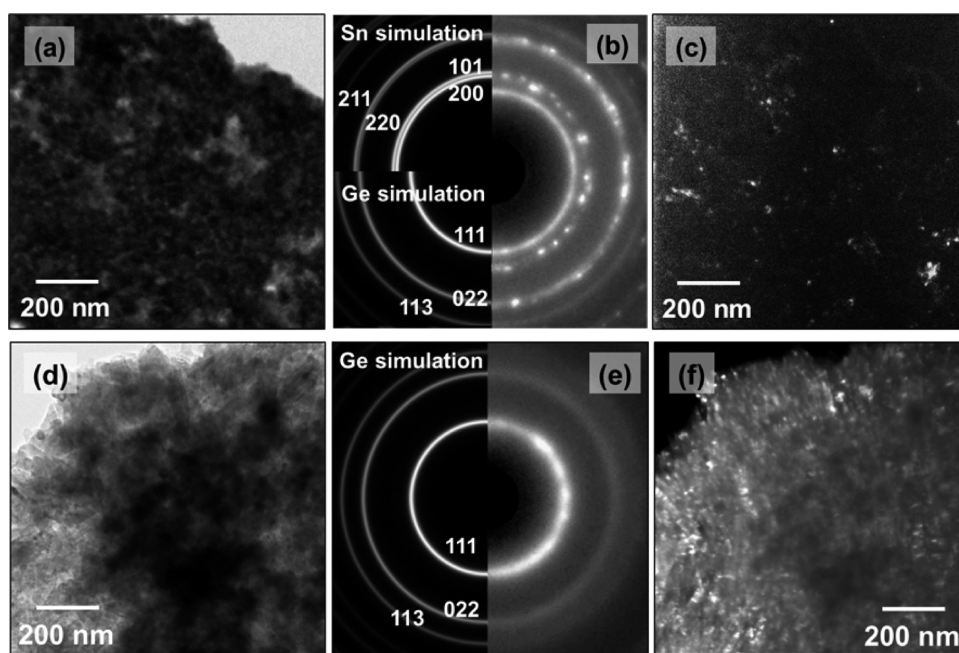


Figure 3. (a–c) Stable cycled microstructures (10 cycles). Desodiated Sn50Ge50, bright field image, indexed SAD pattern, and dark field image taken using a portion of the Sn (200) (101) and Ge (111) ring patterns. In (b) the Sn-induced expansion of the Ge lattice parameter has been taken into account. (d–f) Desodiated Sb50Ge50. The dark field image in (d) was taken using a portion of the Ge (111) ring.

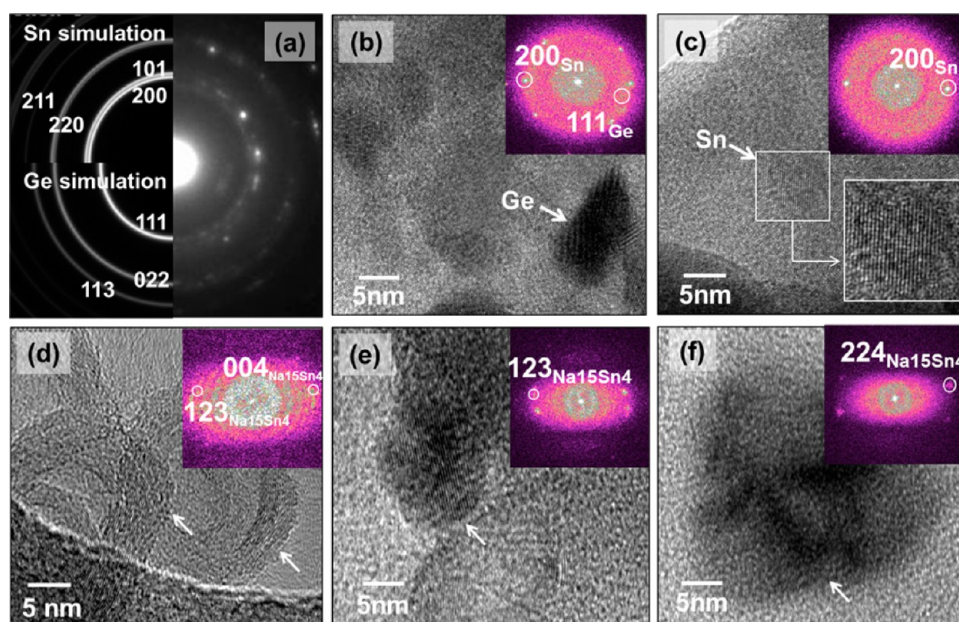


Figure 4. (a–c) SAD and HRTEM micrographs of desodiated Sn50Ge25Sb25 after 10 cycles. HRTEM analysis in (b) and (c) highlights the ~ 5 nm diameter Sn and Ge nanocrystallites dispersed within an amorphous matrix. (d) Sodiated Sn50Ge25Sb25. (e, f) Sodiated Sn80Ge10Sb10, which contains coarser and more spherical $\text{Na}_{15}\text{Sn}_4$ particles and no evidence of a separate Ge phase.

to the indexed SAD pattern shown in Figure 4a, nanocrystalline Sn is present in the material, as evidenced by the (200), (101), and (220)/(211) Sn rings. Well-identifiable ring patterns ascribed to (111), (220), and (311) Ge are present in the SAD as well, giving proof of the presence of nanocrystalline Ge. However from a comparison of the experimental SAD pattern with a simulation, there is no evidence for crystalline Sb.

Figures 4b,c display HRTEM images of this alloy in the desodiated state after 10 cycles. The Sn and Ge nanocrystallites are densely dispersed in an amorphous matrix. As confirmed by EDX spectroscopy, shown in Figure S8, the amorphous matrix is a ternary alloy composed of Sn, Ge, and Sb elements. The amorphous matrix may act as a mechanically buffering phase, allowing for repeated expansion/contraction with

reduced levels of localized fracture. While such effects have been achieved through intelligent design by careful chemical synthesis,^{59–64} here it may occur *in situ* through a natural microstructural evolution. Figure 4d shows this alloy in the sodiated state, highlighting the nonspherical morphology of $\text{Na}_{15}\text{Sn}_4$ intermetallics. Figures 4h,i show HRTEM analysis of the post 10 cycles sodiated $\text{Sn}_{80}\text{Ge}_{10}\text{Sb}_{10}$. The material contains coarser and largely spherical $\text{Na}_{15}\text{Sn}_4$ particles, two representative crystallites being shown by arrows. There is no evidence of a separate Ge phase either from the HRTEM images or from the indexed SADs of the postcycled material (not shown). However an amorphous matrix was also observed in this specimen.

Revisiting the extraordinary results shown in Figure 2, we may begin to understand the origin of the excess capacity beyond the theoretical rule of mixtures by first considering which alloys demonstrate it and which do not. The phenomenon is observed in $\text{Sn}_{50}\text{Ge}_{50}$ and in ternary Sn–Ge–Sb alloys of richer Ge content. It is not observed in $\text{Sb}_{50}\text{Ge}_{50}$ or in $\text{Sn}_{80}\text{Ge}_{10}\text{Sb}_{10}$. It is unlikely that the extra capacity comes from the Sn nanocrystallites since they form the standard terminal $\text{Na}_{15}\text{Sn}_4$ intermetallics in all the sodiated samples. An amorphous structure *per se* would not produce such a capacity enhancement either: $\text{Sb}_{50}\text{Ge}_{50}$ and $\text{Sn}_{80}\text{Ge}_{10}\text{Sb}_{10}$ also contain a large volume fraction of an amorphous phase and yet show no excess capacity beyond the rule of mixtures prediction. We demonstrated that in $\text{Sn}_{50}\text{Ge}_{50}$ and $\text{Sn}_{50}\text{Ge}_{25}\text{Sb}_{25}$ the Ge nanocrystals contain solutionized Sn throughout cycling, with the lattice parameter of Ge being expanded far beyond the equilibrium. Conversely, in cycled $\text{Sn}_{80}\text{Ge}_{10}\text{Sb}_{10}$ the Ge nanocrystals are absent, while in cycled $\text{Sb}_{50}\text{Ge}_{50}$ the Ge crystallites have a lattice parameter near the equilibrium value.

We therefore propose that the measured remarkable capacity enhancement in $\text{Sn}_{50}\text{Ge}_{50}$ and in the alloy-rich ternaries is due to the ability of Ge nanocrystallites alloyed with Sn to sodiate beyond the 1:1 Ge:Na (369 mAhg^{-1}) ratio previously reported for pure Ge electrodes. While a size dependence of phase transitions is experimentally well established for numerous other materials,^{65–68} the lack of capacity enhancement in $\text{Sb}_{50}\text{Ge}_{50}$, or in the nanocolumnar pure Ge electrode employed in a previous study,⁴⁸ suggests that size alone will not drive Ge:Na far beyond 1:1. The equilibrium Ge–Na phase diagram contains an essentially pure Ge phase, a Ge_4Na intermetallic line compound, a GeNa intermetallic line compound, and a GeNa_3 intermetallic line compound whose crystal structure is not known.²⁹ The last phase, which should thermodynamically exist after full discharge, corresponds to a capacity of 1107 mAhg^{-1} . The fact that the capacity of pure Ge never approaches this value

may be a kinetic limitation, normally associated with slow diffusion and/or insurmountable nucleation barriers during room-temperature solid-state phase transformations.⁶⁹

The cycling charge–discharge curves for the ternary alloys show well-defined voltage plateaus, which are typically attributed to energetically distinct two-phase regions. However it is unlikely that the individual $\sim 10 \text{ nm}$ nanocrystallites are able to accommodate a phase boundary *per se*. Thus the two-phase voltage plateau may correspond to a crystallographic dependence of the individual crystallites fully transforming to their sodiated structure. In other words, at a given time the particles with the favorable surface crystal faces/directions will be fully sodiated, while the rest will be unsodiated. A nanocrystalline Ge precipitate with Sn in substitutional solid solution may allow for facile nucleation of one or several Na_xGe_y phases that are inaccessible in the pure state, even if it is not possible to fully reach the 1:3 stoichiometry. Moreover the surrounding amorphous matrix may provide a fast ion diffusion path during sodiation/desodiation, markedly accelerating the kinetics and thus allowing the system to adsorb/release more sodium for a given charge cycle. Such a dependence of the total reversible capacity on rate kinetics is known for hydrogen storage materials, where the same hydride but with an improved catalyst will actually store more hydrogen per sorption cycle.^{70–72}

The absolute value of the reversible capacity of all the materials examined, as a function of cycle number, is shown in Figure 5a. The capacity retention as a fraction of the initial value is shown in Figure S9a, while the associated Coulombic efficiencies are shown in Figure S9b. Elemental Sn, Sb, and Ge, along with the initially crystalline $\text{Sn}_{80}\text{Ge}_{10}\text{Sb}_{10}$ alloy, degrade by far the fastest. Conversely, the more alloyed systems $\text{Sn}_{60}\text{Ge}_{20}\text{Sb}_{20}$, $\text{Sn}_{50}\text{Ge}_{25}\text{Sb}_{25}$, and $\text{Sn}_{33}\text{Ge}_{33}\text{Sb}_{33}$ all cycle fairly well. Table S3 shows the Coulombic efficiency for all alloy electrodes after the first and 50th cycles at 85 mAg^{-1} . For the case of $\text{Sn}_{50}\text{Ge}_{25}\text{Sb}_{25}$ the Coulombic efficiency remains close to 100% during cycles 1–30, listed in Table S4, but begins to decrease afterward, approaching 90% at cycle 50. Such CE values are on par with values reported by others for Sn and Sb elemental and alloy thin films and for Ge films.^{42,48,52} The cycling behavior of the $\text{Sn}_{60}\text{Ge}_{20}\text{Sb}_{20}$ and $\text{Sn}_{50}\text{Ge}_{25}\text{Sb}_{25}$ is analogous, with both alloys demonstrating similar initial and cycle 50 capacity. Likewise, the $\text{Sn}_{33}\text{Ge}_{33}\text{Sb}_{33}$ alloy is stable, but has an overall lower specific capacity.

Electrode failure may be related to several mechanisms. Failure of sodiated Ge electrodes is not well documented in the literature. However for the elemental systems such as Sn and Sb a common source of failure is the occurrence of repeated crystallization events. This leads to an anisotropic stress at two-phase

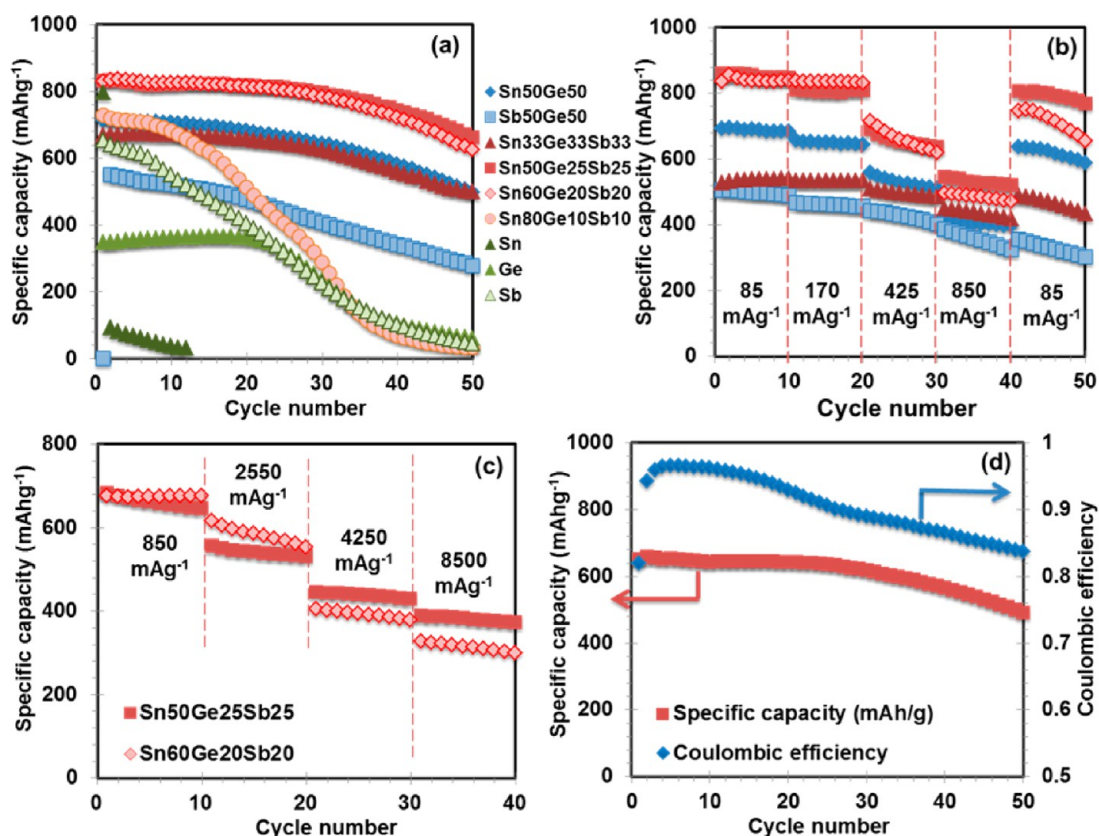


Figure 5. (a) Specific capacity versus cycle number for all materials. Alloys were tested at the same rates as data in Figure 2 and Figure S5. (b, c) Rate capability of binary and ternary alloys. Electrodes in (b) received 50 charge/discharge cycles (data shown in previous panel) prior to the sequential rate testing displayed, while electrodes in (c) were activated for only several cycles and then immediately ramped to 850 mA g⁻¹. (d) Specific capacity and Coulombic efficiency versus cycle number for Sn50Ge25Sb25 electrode cycled at 425 mA g⁻¹ (~0.5C).

boundaries, especially at the substrate/electrode interface. Of Ge, Sn, and Sb elements, Sn is more likely to undergo such transitions. In addition, Sn has the largest volume expansion, with ~425% upon complete sodiation to Na₁₅Sn₄.³⁷ The related stresses would drive the delamination of the electrode from the support for a variety of current collector geometries.

Another contributor to loss of electrical contact is a potential chemical segregation-induced weakening of the electrode–current collector interface. Authors recently reported calculations demonstrating that sodiation of pure Sn phases leads to elastic softening corresponding to a 75% deterioration of the elastic moduli.⁷³ Moreover, for the case of lithium ion battery anodes, failure of similar “film-on-support”-type architectures (Si on Cu) has been both experimentally and theoretically proven to be critically related to a weakening of the mutual interface, in turn due to Li segregation and a change in bonding.⁷⁴ The results shown in Figure 6 are the first direct experimental confirmation of this phenomenon in regard to sodiated (rather than lithiated) systems. Figure 6a shows a TOF-SIMS depth profile of Na and Fe concentration through the thickness of a sodiated Sn50Ge25Sb25 alloy film on a stainless steel substrate after the second sodiation cycle. Clear Na segregation to the film–steel current

collector interface is observed. The HAADF image and thickness-corrected EELS elemental line scan of Na in Sn50Ge25Sb25 after a second sodiation again clearly confirm these segregation phenomena (Figure 6b). Figure 6 also shows FIB cross-section SEM images of (c) pure Sn and (d) Sn50Ge25Sb25 alloy electrodes after 50 cycles. Both films show some delamination from the current collector, but with the case for pure Sn being substantially more severe. In fact according to the FIB image shown, almost the entire pure Sn film is lifted off the current collector, with only the rightmost section in the image making electrical contact.

Upon sodiation, the ternary alloys all undergo an expansion of roughly 300–400%, depending on their total capacity. The alloys have the following approximate characteristics. Sn33Sb33Ge33: 103.3 g mol⁻¹ atoms, max reversible capacity 669 mAhg⁻¹, 2.6 Na atom⁻¹; Sn50Sb25Ge25: 108.0 g mol⁻¹ atoms, max reversible capacity 833 mAhg⁻¹, 3.4 Na atom⁻¹; Sn60Sb20Ge20: 110.1 g mol⁻¹ atoms, max reversible capacity 829 mAhg⁻¹, 3.4 Na atom⁻¹; Sn80Sb10Ge10: 114.4 g mol⁻¹ atoms, max reversible capacity 728 mAhg⁻¹, 3.1 Na atom⁻¹. From a calculation based on the molar volume of each alloy and the molar volume of Na (23.78 cm³ mol⁻¹) the following expansion values are obtained: Sn33Sb33Ge33, 280%; Sn50Sb25Ge25,

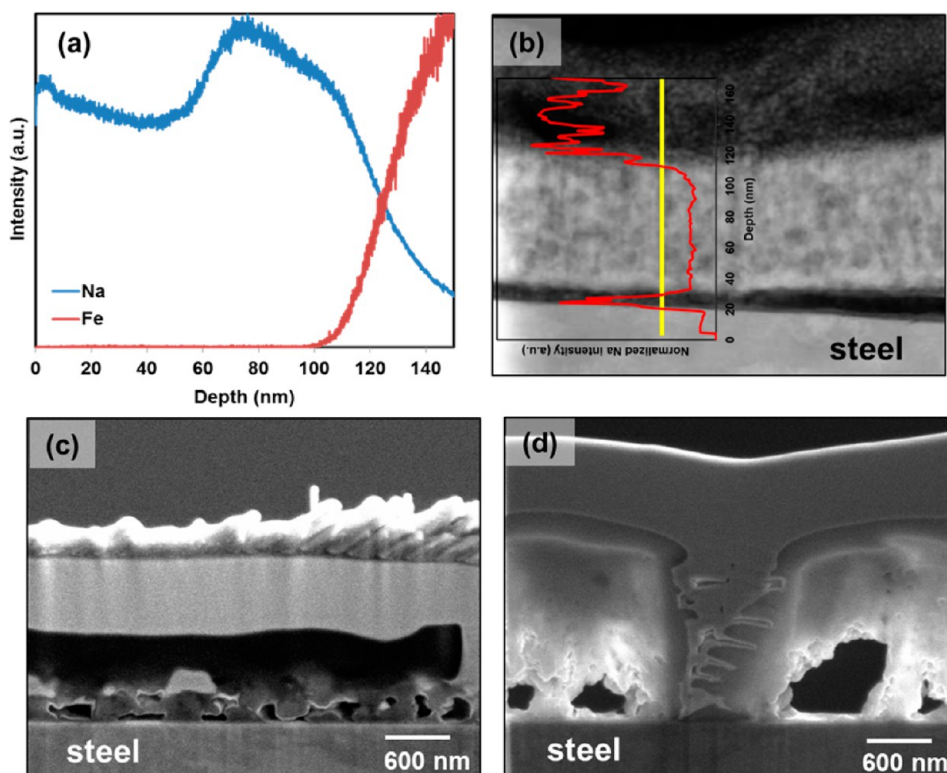


Figure 6. (a) TOF-SIMS depth profile of Na and Fe concentration through the thickness of sodiated Sn50Ge25Sb25 alloy film on stainless steel substrate after the second sodiation. (b) HAADF image and thickness-corrected EELS elemental line scan of Na in Sn50Ge25Sb25 after the second sodiation. (c and d) FIB cross-section SEM images of (c) pure Sn and (d) Sn50Ge25Sb25 alloy electrodes after 50 cycles.

380%; Sn60Sb20Ge20, 380%; Sn80Sb10Ge10, 340%. Thus, it can be concluded that the alloys with the highest capacity also undergo the largest expansion upon sodiation and that the cycling lifetime does not depend on minimizing the volume changes. This leads us to hypothesize that the heavily alloyed systems actually suffer less from Na-induced interfacial-softening tendency despite the fact that Na segregation still occurs. Classic metallurgical alloy design would rather contribute substitutional solid solution strengthening, an increased resistance to crystallization, and a multiphase nanocomposite microstructure that gives both strength and ductility, leading to the observed increased resistance to interfacial delamination.

One successful way to improve the cycling stability of materials with exceptionally large sodiation/lithiation expansion is to form nanocomposites with lower-expansion materials such as amorphous carbon,^{38,75} empty space,^{61–79} Cu,³⁷ or nanoscale films of Al and atomic-scale films of TiO₂ and TiN.^{80–82} These either buffer the massive volume changes (carbon, empty space) or mechanically scaffold (Cu, Al, TiO₂, TiN) the primary active material, thus preventing its disintegration. For the case of the cyclically stable ternary Sn–Ge–Sb alloys, the amorphous matrix may accomplish a similar goal, surrounding the highly Na-active Sn-alloyed Ge and unalloyed Sn nanocrystallites and

mechanically preventing their loss of electrical contact with the current collector.

The electrolyte solvents used in studies of NIB anodes are generally the same as for LIB and in our case consisted of a mixture of ethylene carbonate (EC) and diethyl carbonate (DEC). The operating potential of a NIB anode is slightly more positive than for LIB but still well below the onset potential of electrolyte reduction for this type of cyclic carbonate compound, forming a so-called solid electrolyte interphase (SEI), which is very similar for Na or Li electrolyte salts.¹⁷ Since reduction of the solvent molecules to Na₂CO₃, Na alkyl carbonates, and Na alkoxides consumes electrons irreversibly, this will reduce the Coulombic efficiency. Indeed, the first cycle CE that we found was generally around 60–70%. Formation of an SEI layer will also increase the charge transfer resistance and thereby increase the overpotential^{83–85} and reduce the capacity that can be extracted at a given current density. For materials that exhibit high expansion upon cycling, the SEI will fracture and expose fresh material to the electrolyte, leading to a buildup of an ever thicker surface layer. SEI accumulation in cracks or voids can lead to detachment of active material from the rest of the active mass and/or delamination from a substrate.^{74,75,86} For thin films this problem is somewhat alleviated, as expansion is confined to the direction perpendicular to the substrate. Indeed, we found CE

TABLE 1. Comparison of Our Best-Performing Materials with Previously Published Sn-, Sb-, and Ge-Based NIB Anodes, as Well as Some Carbon Nanostructures, in Terms of Capacity and Rate Capability

electrodes	cycling capacity, mAhg ⁻¹ (current density)			rate capability, mAhg ⁻¹ (current density)	
	1st	10th	50th		
Sn50Ge25Sb25	833	821	662	658	381
Sn60Ge20Sb20	829	826	625	675	313
	(85 mAg ⁻¹)	(85 mAg ⁻¹)	(85 mAg ⁻¹)	(85 mAg ⁻¹)	(85 mAg ⁻¹)
	(55 mAcm ⁻²)	(55 mAcm ⁻²)	(55 mAcm ⁻²)	(550 mAcm ⁻²)	(5500 mAcm ⁻²)
	(0.1C)	(0.1C)	(0.1C)	(1C)	(10C)
Sn/C nanocomposite ⁷⁵	470 (50 mAg ⁻¹)	270 (50 mAg ⁻¹)	N/A	N/A	N/A
Sn—Cu nanocomposite ³⁷	~250 (169 mAg ⁻¹)	~420 (169 mAg ⁻¹)	~460 (169 mAg ⁻¹)	182 (847 mAg ⁻¹)	126 (1694 mAg ⁻¹)
Sn—SnS—C composite ³⁸	~430 (100 mAg ⁻¹)	~425 (100 mAg ⁻¹)	~450 (100 mAg ⁻¹)	~350 (800 mAg ⁻¹)	N/A
Sn—C composite ³⁸	~240 (100 mAg ⁻¹)	~280 (100 mAg ⁻¹)	~220 (100 mAg ⁻¹)	~150 (800 mAg ⁻¹)	N/A
nanocolumnar germanium thin films ⁴⁸	~480 (74 mAg ⁻¹)	~470 (74 mAg ⁻¹)	~460 (74 mAg ⁻¹)	380 (370 mAg ⁻¹)	170 (10 000 mAg ⁻¹)
Sb/C fibers ⁴¹	~450 (100 mAg ⁻¹)	~400 (100 mAg ⁻¹)	~420 (100 mAg ⁻¹)	~300 (1000 mAg ⁻¹)	~100 (6000 mAg ⁻¹)
tin-coated viral nanoforests ⁵⁶	~770 (50 mAg ⁻¹)	~580 (50 mAg ⁻¹)	~470 (50 mAg ⁻¹)	N/A	N/A
Sn nanoparticles with Al ₂ O ₃ nanoglue ⁹¹	~620 (N/A)	~680 (N/A)	N/A	N/A	N/A
Sn-film electrode in NaFSA KFSA ³⁰	~330 (0.6 mAcm ⁻²)	~300 (0.6 mAcm ⁻²)	N/A	N/A	N/A
mesoporous C/Sn composite ⁵	~300 (20 mAg ⁻¹)	~250 (20 mAg ⁻¹)	N/A	~70 (800 mAg ⁻¹)	~60 (1000 mAg ⁻¹)
Sn @ wood fibers ³¹	~350 (84 mAg ⁻¹)	~220 (84 mAg ⁻¹)	~250 (84 mAg ⁻¹)	~75 (840 mAg ⁻¹)	N/A
SnSb/C nanocomposite ⁴	~570 (100 mAg ⁻¹)	~520 (100 mAg ⁻¹)	435 (100 mAg ⁻¹)	~280 (1000 mAg ⁻¹)	N/A
hollow carbon nanowires ¹⁵	251 (50 mAg ⁻¹)	~250 (50 mAg ⁻¹)	~240 (50 mAg ⁻¹)	149 (500 mAg ⁻¹)	N/A
carbon nanofibers ¹⁶	~200 (200 mAg ⁻¹)	~180 (200 mAg ⁻¹)	175 (200 mAg ⁻¹)	~80 (500 mAg ⁻¹)	~60 (2000 mAg ⁻¹)
Sb—C nanocomposite ⁴⁰	~610 (100 mAg ⁻¹)	~600 (100 mAg ⁻¹)	~600 (100 mAg ⁻¹)	~500 (1000 mAg ⁻¹)	~300 (2000 mAg ⁻¹)
Cu ₂ Sb thin films ⁴⁴	~280 (100 μ Acm ⁻²)	~270 (100 μ Acm ⁻²)	~50 (100 μ Acm ⁻²)	~230 (100 μ Acm ⁻²)	N/A
AlSb thin films ⁴⁵	~490 (40 μ Acm ⁻²)	~350 (40 μ Acm ⁻²)	~250 (40 μ Acm ⁻²)	~100 (40 μ Acm ⁻²)	N/A
Mo ₃ Sb ₇ thin films ⁴⁶	~330 (0.6 mAcm ⁻²)	~340 (0.6 mAcm ⁻²)	~300 (0.6 mAcm ⁻²)	~300 (0.6 mAcm ⁻²)	~110 (18 mAcm ⁻²)
Sb/MWCNT nanocomposite ⁴⁷	~500 (100 mAg ⁻¹)	~500 (100 mAg ⁻¹)	~450 (100 mAg ⁻¹)	~350 (1000 mAg ⁻¹)	~250 (2000 mAg ⁻¹)
SnO ₂ @MWCNT nanocomposite ⁹²	~500 (N/A) (0.1C)	~450 (N/A) (0.1C)	~380 (N/A) (0.1C)	~310 (N/A) (0.5C)	N/A
Sb ₂ O ₃ thin films ⁹³	~980 (N/A) (0.1C)	~500 (N/A) (0.1C)	N/A	N/A	N/A
Sn _{0.3} C _{0.3} C _{0.4} nanocomposite ³⁴	~400 (N/A) (0.04C)	~200 (N/A) (0.04C)	N/A	N/A	N/A
porous Sb/Cu ₂ Sb anode ⁴²	~617 (N/A) (0.1C)	~600 (N/A) (0.1C)	~550 (N/A) (0.1C)	~470 (N/A) (1C)	~280 (N/A) (5C)
SnO ₂ —RGO nanocomposite ⁹⁴	407 (100 mAg ⁻¹)	~500 (100 mAg ⁻¹)	~400 (100 mAg ⁻¹)	~200 (500 mAg ⁻¹)	~120 (1000 mAg ⁻¹)
Cu ₆ Sn ₅ ³⁶	160 (7.9 mAcm ⁻²)	75 (7.9 mAcm ⁻²)	N/A	N/A	N/A
Sn ₂₅ Cu ₃₁ C ₄₄ ³⁶	135 (0.1C)	120 (0.1C)	117 (0.1C)	N/A	N/A
Sn ₃₉ Cu ₄₆ C ₁₅ ³⁵	350 (0.1C)	330 (0.1C)	160 (0.1C)	465 (600 mAg ⁻¹)	337 (3000 mAg ⁻¹)
Sb—C nanofibers ⁹⁵	495 (200 mAg ⁻¹)	~500 (200 mAg ⁻¹)	~500 (200 mAg ⁻¹)	N/A	N/A
ALD-Al ₂ O ₃ coated Sn nanoparticles ⁹⁶	625 (N/A)	650 (N/A)	N/A	N/A	N/A

close to 100% for Sn50Sb25Ge25 in cycles 2–30. However, expansion is so severe for NIB alloying anodes (up to a factor 5.2 for pure Sn and comparable expansion ratios were estimated based on our measured capacities) that beyond cycle 30 the CE and reversible capacity starts to drop.

Modifications to the electrolyte have been highly successful in extending the lifetime of some high-expansion electrode materials. It has been shown that Si nanowires can be cycled thousands of times without significant degradation in electrolyte solvents that are highly resistant to reduction such as 1,3-dioxolane, despite 280% volume expansion.⁸⁷ Alternatively, addition of fluoroethylene carbonate (FEC) to conventional electrolyte mixtures has also been found to increase electrode lifetime^{40,41,88} and modify the SEI layer.^{89,90} Compared to standard carbonate mixtures, SEI formed from FEC is found to be very thin and contain large amounts of a polyene compound⁸³ that can passivate the electrode surface. High polymeric content would

make the SEI more elastic compared to one composed entirely of Li salts and less prone to fracture. This is especially important for materials that expand by extremely large amounts such as Sn and Sn-based alloys that we studied here. We would expect that the CE and cycling performance of our materials could be much improved by electrolyte modification.

Binary and ternary alloy electrodes were subjected to rate-capability tests, with the results being shown in Figure 5b and c. Capacity retention as a fraction of the measured capacities is plotted in Figure S9a. Samples in Figure 5b received 50 charge/discharge cycles (shown in Figure 5a) prior to the rate testing, while alloys in Figure 5c were activated at 85 mAg⁻¹ for only several cycles and then rate tested. The degradation incurred in cycles 1–50 explains the capacity discrepancy at 850 mAg⁻¹ between the two plots. Both Sn50Ge25Sb25 and Sn60Ge20Sb20 show excellent rate capability, with capacities of 381 and 313 mAhg⁻¹ being retained at a charge/discharge rate near 10C.

As shown in Figure 5d, the Sn50Ge25Sb25 electrode revealed an initial reversible specific capacity of 653 and 491 mAhg⁻¹ after 50 charge–discharge cycles at 425 mAg⁻¹, indicating excellent cycling performance of this alloy at a relatively high cycling rate of ~0.5C.

The electrochemical impedance spectra (EIS) Nyquist plots of the Sn50Ge25Sb25 alloy in the as-synthesized state and after 50 cycles at 85 mAg⁻¹ are shown in Figure S10. As indicated in Figure S10b, cycled Sn50Ge25Sb25 has a low equivalent series resistance but that is generally on par with the elemental electrodes. This implies that the fast rate capability of the alloy is attributable to the facile phase transformation kinetics, rather than to an enhanced electrical conductivity of the material *per se*. It is instructive to compare the performance of the Sn–Ge–Sb electrodes with the best systems reported in the scientific literature. Table 1 compares our results with the state-of-the-art in previously published research on Sn-based NIB anode materials. It can be concluded that Sn50Ge25Sb25 and Sn60Ge20Sb20 electrodes exhibit one of the most promising capacity–rate capability combinations, with performance at 10C being especially desirable.

Finally it is important to point out that while physical vapor co-deposition (co-sputtering) of alloy films represents a repeatable and compositionally accurate method for rapidly screening new materials, the microstructures discovered in this study are attainable through more “bulk” methods as well. High-energy mechanical alloying and rapid solidification are two well-known techniques for achieving a range of nonequilibrium microstructures that are in-practice stable during service. Co-milling is especially effective for the relatively soft metallic systems, such as those based on Sn or Sb, that undergo significant cold-welding and interdiffusion rather than pulverizing. For instance, metastable Ge–12 atom % Sn⁹⁷ and 34 atom % Ge⁹⁸ substitutional solid solutions have already been synthesized by high-energy mechanical milling, although the authors did not employ the resultant structures for electrochemical purposes. Rapid solidification (melt

spinning) has also been recently employed to produce metastable SnTe–Se thermoelectric alloys,⁹⁹ as well as Sn–Ge lithium ion battery anodes with exceptional charge storage capacities and cycling stability.¹⁰⁰ Neither co-milling nor rapid solidification methods suffer from practical engineering concerns of limited mass loadings or the need for planar geometries and are therefore readily scalable to the desired battery application. In order to limit phase segregation in larger structures, a fourth element possessing a strong affinity for Sn, Sb, and Ge may also be added. This was successfully achieved through the addition of S or Se into the nonequilibrium microstructures of Sn–Co–C nanocomposites, which were then sufficiently stable in bulk form as to be utilized for cyclable sodium ion battery anodes.³⁴

CONCLUSIONS

This study reports the electrochemical charge/discharge cycling behavior of Sn–Ge–Sb, Sn–Ge, and Sb–Ge alloy thin films for use as sodium ion battery anodes, testing pure Sn, Ge, and Sb films as well. The measured reversibly capacities of Sn80Ge10Sb10, Sn60Ge20Sb20, Sn50Ge25Sb25, and Sn33Ge33Sb33 are 728, 829, 833, and 669 mAhg⁻¹. With the exception of Sn80Ge10Sb10, these values are considerably above the weighted average combination of the elemental capacities, which should be 800, 743, 714, and 664 mAhg⁻¹, respectively. Of all the compositions investigated, Sn50Ge25Sb25 demonstrates the best overall cycling performance, with 662 mAhg⁻¹ of capacity remaining after 50 cycles. The alloy also offers exquisite rate capability, delivering a stable cycling capacity of 658 and 381 mAhg⁻¹ at 850 and 8500 mAg⁻¹, respectively. We employ conventional TEM and HRTEM to investigate the materials' cycling microstructures, the optimum system being a composite of 10–15 nm Sn and Ge(Sn) crystals nanodispersed in an amorphous matrix. A hypothesis put forth is that the capacity enhancement is due to the unique ability of Ge nanocrystallites that are heavily alloyed with Sn to sodiate beyond the 1:1 Ge:Na (369 mAhg⁻¹) ratio previously reported for pure Ge electrodes.

EXPERIMENTAL PROCEDURE

Target composition 100 nm films were (co)sputtered onto polished stainless steel substrates (battery spacers) at room temperature (ATC Orion 8, AJA International Inc.). Sb and Ge deposition were carried out using radio frequency-magnetron sputtering, while Sn deposition was performed by dc-magnetron sputtering. Depositions were performed with continuous substrate rotation in the presence of Ar gas with 5 N purity at a sputtering pressure of 4 mTorr, with a maximum base pressure of 5×10^{-8} Torr. The deposition rates were adjusted for stoichiometry, being in the range 0.04–0.39 nm s⁻¹. The primary approach for confirming film thicknesses depended on a series of *ex situ* deposition calibrations cross-checked against *in situ* calibrations, film weight measurements, and XPS. For a range of gun powers relevant to the deposition conditions, a series of elemental films were deposited at varying

times with thicknesses up to 1.5 μm. Film thicknesses were then analyzed using a standard profilometer approach, with the deposition rate per given power being back-calculated. These results were cross-checked against an *in situ* deposition rate monitor held in the plane of the substrate (instead of the battery substrate), using known tooling factors for each element. To ensure that resputtering did not affect the final alloy film stoichiometry or thickness (it should not since the atomic weights of the elements are not that divergent), the weight of the alloy film was compared to the rule of mixtures weight that would be expected for the 100 nm film thickness employed for all materials. High-resolution FE-SEM was employed as a secondary confirmation tool for reporting the film thicknesses. Film compositions were further confirmed using X-ray photoelectron spectroscopy (XPS) and are listed in atomic %; for example, Sn50Ge25Sb25 is 50 atom % Sn–25 atom % Ge–25 atom % Sb.

Na half-cells were assembled using Na metal foil as the counter electrode and polyethylene separators (MTI Corporation, porosity of 36–44% and average 0.03 μm pore size); 316 stainless steel spacer disks (MTI Corporation), with a diameter and thickness of 15.8 mm and 0.5 mm, respectively, were used as the substrates for thin film deposition. Prior to deposition, the spacers were polished down to 5 μm SiC polishing paper (Allied High Tech Products, Inc.). The substrates were then cleaned by sonication in acetone, 2-propanol, and Milli-Q water and were finally dried. The spacers were weighted before and after deposition. The microbalance employed (Mettler Toledo, XP6U) had a manufacturer quoted 0.1 μg accuracy. For each composition, 3–6 samples were electrochemically tested to obtain a mean value of reversible capacity. Extended cycling testing was performed on 2 or 3 specimens per composition. Table S1 shows the average weight and standard deviation for each composition based on 6 different samples. Table S2 shows the XPS and EDXS results of as-synthesized alloy electrodes. The EDXS results contain approximately $\pm 10\%$ error. In general more quantitative validity may be attributed to the XPS results. The raw XPS and EDXS data are shown in Figures S1 and S2.

As an electrolyte, 1 M sodium perchlorate (NaClO_4 , Alfa Aesar, 98–102% purity) salt in ethylene carbonate (Alfa Aesar: 99% purity)–diethyl carbonate (Alfa Aesar: >99% purity) (1:1 by volume) was used. The assembly process was carried out in an argon-filled glovebox in which oxygen and moisture concentration levels were kept below 0.2 ppm. Galvanostatic charge–discharge tests were performed on a BT2000 Arbin potentiostat at a potential range of 0.01–2 V versus Na/Na^+ and a constant current density. Current densities were based on the accurately measured final weight of the films. We employ the usual definition of a reversible capacity being the capacity at first charge (desodiation). Electrochemical impedance spectroscopy measurement was conducted on a Solartron 1470E multi-channel potentiostat in a frequency range of 10 MHz to 0.01 Hz at open-circuit potential condition with an ac perturbation of 10 mV. Na batteries were disassembled in order to do post-cycling characterization of the microstructure. Cycled electrodes were soaked and rinsed in acetonitrile (Fisher Scientific, >95% purity) and kept overnight in the glovebox to remove residual electrolyte.

As-deposited and cycled samples were characterized using transmission electron microscopy (TEM; JEOL 2010 and JEOL JEM 2100, both at 200 kV). Electron diffraction patterns were simulated using the commercial software Crystal Maker and open-source software Diffraction Ring Profiler,⁵⁰ with the input of known space group information of the relevant phases, such as Sn ($I4_1/amd$, 5.8197, 5.8197, 3.1749, Wyckoff position: 4a), Ge ($Fd3m$, 5.6578, 5.6578, 5.6578, Wyckoff position: 8a), Sb ($R\bar{3}m$, 4.5066, 4.5066, 4.5066, Wyckoff position: 36i), $\text{Na}_{15}\text{Sn}_4$ ($I43d$, 13.16, 13.16, 13.16, Wyckoff positions $\text{Sn}1:16c$, $\text{Na}1:12a$, $\text{Na}2:48e$), and Na_3Sb ($P6_3/mmc$, 5.3550, 5.3550, 9.4960, Wyckoff positions $\text{Sb}1:2c$, $\text{Na}1:2b$, $\text{Na}2:12k$). The diffraction ring profiler integrates the selected area diffraction ring pattern intensities to accurately calculate the center point of each ring. High-resolution TEM (HRTEM) measurements were conducted using scanning TEM (STEM) (JEOL 2200FS, 200 kV) with a nominal beam size of 0.5 nm. Electron energy loss spectroscopy (EELS) analysis was also conducted using a 200 kV JEOL 2200FS scanning TEM with a nominal beam size of 0.5 nm. High-angle annular dark field (HAADF) images were also recorded. Digital Micrograph (Gatan, Inc.) was employed for signal collection and data extraction from EELS spectra. The Na spectrum was extracted by integrating over low loss edges of Na at 30–40 eV. Typical current densities for HRTEM imaging were 13.15 pA cm^{-2} at 400 K and 16.72 pA cm^{-2} at 500 K.

Crystal structures of as-deposited thin films were characterized by X-ray diffraction (XRD) on a Bruker AXS diffractometer with $\text{Cu K}\alpha$ radiation ($\lambda = 1.5406 \text{ \AA}$) (Bruker Discover 8). The diffractometer is equipped with a HiStar general area two-dimensional detection system with a sample–detector distance of 15 cm. Phase identification was performed employing the XRD database on EVA software. The presented XRD patterns were obtained by subtracting the pattern of the substrate from the composite. To achieve this, we performed XRD on both the

stainless steel substrate and on the deposited thin film on the substrate, employing identical scanning conditions. The mathematical subtraction was performed using EVA commercial software. Cross-sectional samples of cycled materials were obtained using a Hitachi NB5000 dual-beam focused ion beam/scanning electron microscope (FIB/SEM). To prepare FIB samples, a proper area from the bulk of the sample was selected using SEM. A thin layer of carbon and tungsten were then deposited on top of the area. Using FIB and a microsample manipulator, the selected volume was finally isolated, lifted out, and placed on a Cu five-post grid.

The as-synthesized and cycled thin films were also analyzed using EDX spectroscopy with scanning electron microscopy on a Hitachi FESEM S-5500. XPS measurements were conducted on an ULTRA (Kratos Analytical) spectrometer under ultrahigh vacuum (10^{-9} Torr), using monochromatic $\text{Al K}\alpha$ radiation ($h\nu = 1486.6 \text{ eV}$) operated at 210 W. The high-resolution spectra were collected with an energy window of 20 eV. The XPS data were analyzed using CasaXPS software. The sodiated $\text{Sn}_{50}\text{Ge}_{25}\text{Sb}_{25}$ thin film electrode was depth analyzed using a time-of-flight secondary ion mass spectrometry (TOF-SIMS) instrument (ION-TOF GmbH). The analysis chamber was kept at a pressure of less than 5×10^{-9} mbar, and a 25 kV Bi^+ ion source was used for analysis. For sputtering, 1 kV O_2^+ ions with a current of $\sim 34 \text{ nA}$ were also used with the rate of $\sim 0.06 \text{ nm/s}$. The analysis and sputtering areas were $40 \mu\text{m} \times 40 \mu\text{m}$ and $200 \mu\text{m} \times 200 \mu\text{m}$, respectively.

Prior to XRD, XPS, and TOF-SIMS analysis the samples were covered and sealed with Parafilm in a glovebox to avoid exposure to air. Next, the airtight sample holder was transferred to the XRD instrument for measurement of the XRD patterns. For TEM, the samples were quickly transferred into the TEM, reducing its air exposure to around 20 s. TEM analysis did not reveal excessive oxide formation on the surfaces, and we were able to perform quantitative HRTEM and analytical TEM without interference from the oxide.

Conflict of Interest: The authors declare no competing financial interest.

Acknowledgment. This work was sponsored by NSERC Discovery.

Supporting Information Available: Figures S1–S10 and Tables S1–S4 as described in the text. This material is available free of charge via the Internet at <http://pubs.acs.org>.

REFERENCES AND NOTES

- Slater, M. D.; Kim, D.; Lee, E.; Johnson, C. S. Sodium Ion Batteries. *Adv. Funct. Mater.* **2013**, 23, 947–958.
- Ellis, B. L.; Nazar, L. F. Sodium and Sodium-Ion Energy Storage Batteries. *Curr. Opin. Solid State Mater. Sci.* **2012**, 16, 168–177.
- Palomares, V.; Serras, P.; Villaluenga, I.; Hueso, K. B.; Carretero-Gonzalez, J.; Rojo, T. Na Ion Batteries, Recent Advances and Challenges to Become Low Cost Energy Storage Systems. *Energ. Environ. Sci.* **2012**, 5, 5884–5901.
- Xiao, L. F.; Cao, Y. L.; Xiao, J.; Wang, W.; Kovarik, L.; Nie, Z. M.; Liu, J. High Capacity, Reversible Alloying Reactions in SnSb/C Nanocomposites for Na-Ion Battery Applications. *Chem. Commun.* **2012**, 48, 3321–3323.
- Xu, Y. H.; Zhu, Y. J.; Liu, Y. H.; Wang, C. S. Electrochemical Performance of Porous Carbon/Tin Composite Anodes for Sodium-Ion and Lithium-Ion Batteries. *Adv. Energ. Mater.* **2013**, 3, 128–133.
- Kim, S. W.; Seo, D. H.; Ma, X. H.; Ceder, G.; Kang, K. Electrode Materials for Rechargeable Sodium-Ion Batteries: Potential Alternatives to Current Lithium-Ion Batteries. *Adv. Energ. Mater.* **2012**, 2, 710–721.
- Palomares, V.; Casas-Cabanas, M.; Castillo-Martinez, E.; Han, M. H.; Rojo, T. Update on Na-Based Battery Materials. A Growing Research Path. *Energ. Environ. Sci.* **2013**, 6, 2312–2337.
- Chevrier, V. L.; Ceder, G. Challenges for Na-Ion Negative Electrodes. *J. Electrochem. Soc.* **2011**, 158, A1011–A1014.

9. Pan, H. L.; Hu, Y. S.; Chen, L. Q. Room-Temperature Stationary Sodium-Ion Batteries for Large-Scale Electric Energy Storage. *Energ. Environ. Sci.* **2013**, *6*, 2338–2360.
10. Pourbaix, M. *Atlas of Electrochemical Equilibria in Aqueous Solutions*; National Association of Corrosion Engineers, 1974.
11. Wibowo, R.; Aldous, L.; Jones, S. E. W.; Compton, R. G. The Electrode Potentials of the Group I Alkali Metals in the Ionic Liquid N-butyl-N-methylpyrrolidinium bis-(trifluoromethylsulfonyl)imide. *Chem. Phys. Lett.* **2010**, *492*, 276–280.
12. Ha, K.-H.; Woo, S. H.; Mok, D.; Choi, N.-S.; Park, Y.; Oh, S. M.; Kim, Y.; Kim, J.; Lee, J.; Nazzari, L. F.; Lee, K. T. $\text{Na}_{4-x}\text{M}_{2+x/2}(\text{P}_2\text{O}_7)_2$ ($2/3 \leq x \leq 7/8$, $\text{M} = \text{Fe}, \text{Fe}_{0.5}\text{Mn}_{0.5}, \text{Mn}$): A Promising Sodium Ion Cathode for Na-Ion Batteries. *Adv. Energ. Mater.* **2013**, *3*, 770–776.
13. Tripathi, R.; Gardiner, G. R.; Islam, M. S.; Nazar, L. F. Alkali-Ion Conduction Paths in LiFeSO_4F and NaFeSO_4F Favorite-Type Cathode Materials. *Chem. Mater.* **2011**, *23*, 2278–2284.
14. Metrot, A.; Guerard, D.; Billaud, D.; Herold, A. New Results about the Sodium-Graphite System. *Synth. Met.* **1979**, *80*, 1, 363.
15. Cao, Y.; Xiao, L.; Sushko, M. L.; Wang, W.; Schwenzer, B.; Xiao, J.; Nie, Z.; Saraf, L. V.; Yang, Z.; Liu, J. Sodium Ion Insertion in Hollow Carbon Nanowires for Battery Applications. *Nano Lett.* **2012**, *12*, 3783–3787.
16. Luo, W.; Schardt, J.; Bommer, C.; Wang, B.; Razink, J.; Simonsen, J.; Ji, X. Carbon Nanofibers Derived from Cellulose Nanofibers as a Long-Life Anode Material for Rechargeable Sodium-Ion Batteries. *J. Mater. Chem. A* **2013**, *1*, 10662.
17. Komaba, S.; Murata, W.; Ishikawa, T.; Yabuuchi, N.; Ozeki, T.; Nakayama, T.; Ogata, A.; Gotoh, K.; Fujiwara, K. Electrochemical Na Insertion and Solid Electrolyte Interphase for Hard-Carbon Electrodes and Application to Na-Ion Batteries. *Adv. Funct. Mater.* **2011**, *21*, 3859.
18. Ding, J.; Wang, H.; Li, Z.; Kohandehghan, A.; Cui, K.; Xu, Z.; Zahiri, B.; Tan, X.; Memarzadeh, E.; Olsen, B. C.; Mitlin, D. Carbon Nanosheet Frameworks Derived from Peat Moss as High Performance Sodium Ion Battery Anodes. *ACS Nano* **2013**, *7*, 11004–11015.
19. Shao, Y. Y.; Xiao, J.; Wang, W.; Engelhard, M.; Chen, X. L.; Nie, Z. M.; Gu, M.; Saraf, L. V.; Exarhos, G.; Zhang, J. G.; Liu, J. Surface-Driven Sodium Ion Energy Storage in Nanocellular Carbon Foams. *Nano Lett.* **2013**, *13*, 3909–3914.
20. Ponrouch, A.; Goni, A. R.; Palacin, M. R. High Capacity Hard Carbon Anodes for Sodium Ion Batteries in Additive Free Electrolyte. *Electrochem. Commun.* **2013**, *27*, 85–88.
21. Senguttuvan, P.; Rousse, G.; Seznec, V.; Tarascon, J. M.; Palacin, M. R. $\text{Na}_2\text{Ti}_3\text{O}_7$: Lowest Voltage Ever Reported Oxide Insertion Electrode for Sodium Ion Batteries. *Chem. Mater.* **2011**, *23*, 4109–4111.
22. Zhao, L.; Pan, H. L.; Hu, Y. S.; Li, H.; Chen, L. Q. Spinel Lithium Titanate ($\text{Li}_4\text{Ti}_5\text{O}_{12}$) as Novel Anode Material for Room-Temperature Sodium-Ion Battery. *Chin. Phys. B* **2012**, *21*, 028201.
23. Pan, H. L.; Lu, X.; Yu, X. Q.; Hu, Y. S.; Li, H.; Yang, X. Q.; Chen, L. Q. Sodium Storage and Transport Properties in Layered $\text{Na}_2\text{Ti}_3\text{O}_7$ for Room-Temperature Sodium-Ion Batteries. *Adv. Energ. Mater.* **2013**, *3*, 1186–1194.
24. Rudola, A.; Saravanan, K.; Mason, C. W.; Balaya, P. $\text{Na}_2\text{-Ti}_3\text{O}_7$: An Intercalation Based Anode for Sodium-Ion Battery Applications. *J. Mater. Chem. A* **2013**, *1*, 2653–2662.
25. Xu, Y.; Lotfabad, E. M.; Wang, H. L.; Farbod, B.; Xu, Z. W.; Kohandehghan, A.; Mitlin, D. Nanocrystalline Anatase TiO_2 : A New Anode Material for Rechargeable Sodium Ion Batteries. *Chem. Commun.* **2013**, *49*, 8973–8975.
26. Kim, K.-T.; Ali, G.; Chung, K. Y.; Yoon, C. S.; Yashiro, H.; Sun, Y. K.; Sun, Y.-K.; Lu, J.; Amine, K.; Myung, S.-T. Anatase Titania Nanorods as an Intercalation Anode Material for Rechargeable Sodium Batteries. *Nano Lett.* **2014**, *14* (2), 416–422.
27. Wu, L.; Buchholz, D.; Bresser, D.; Chagas, L. G.; Passerini, S. Anatase TiO_2 Nanoparticles for High Power Sodium-Ion Anodes. *J. Power Sources* **2014**, *251*, 379–385.
28. Kim, H.; Jeong, G.; Kim, Y.-U.; Kim, J.-H.; Park, C.-M.; Sohn, H.-J. Metallic Anodes for Next Generation Secondary Batteries. *Chem. Soc. Rev.* **2013**, *42*, 9011–9034.
29. Okamoto, H. *Desk Handbook of Phase Diagrams for Binary Alloys*; ASM International, 2000.
30. Yamamoto, T.; Nohira, T.; Hagiwara, R.; Fukunaga, A.; Sakai, S.; Nitta, K.; Inazawa, S. Charge-Discharge Behavior of Tin Negative Electrode for a Sodium Secondary Battery Using Intermediate Temperature Ionic Liquid Sodium Bis(Fluorosulfonyl) Amide-Potassium Bis(fluorosulfonyl)-amide. *J. Power Sources* **2012**, *217*, 479–484.
31. Zhu, H. L.; Jia, Z.; Chen, Y. C.; Weadock, N.; Wan, J. Y.; Vaaland, O.; Han, X. G.; Li, T.; Hu, L. B. Tin Anode for Sodium-Ion Batteries Using Natural Wood Fiber as a Mechanical Buffer and Electrolyte Reservoir. *Nano Lett.* **2013**, *13*, 3093–3100.
32. Ellis, L. D.; Hatchard, T. D.; Obrovac, M. N. Reversible Insertion of Sodium in Tin. *J. Electrochem. Soc.* **2012**, *159*, A1801–A1805.
33. Baggetto, L.; Ganesh, P.; Meisner, R. P.; Unocic, R. R.; Jumas, J. C.; Bridges, C. A.; Veith, G. M. Characterization of Sodium Ion Electrochemical Reaction with Tin Anodes: Experiment and Theory. *J. Power Sources* **2013**, *234*, 48–59.
34. Ellis, L. D.; Ferguson, P. P.; Obrovac, M. N. Sodium Insertion into Tin Cobalt Carbon Active/Inactive Nanocomposite. *J. Electrochem. Soc.* **2013**, *160*, A869–A872.
35. Thorne, J. S.; Dunlap, R. A.; Obrovac, M. N. Cu_6Sn_5 Active/Inactive Nanocomposite Negative Electrodes for Na-Ion Batteries. *Electrochim. Acta* **2013**, *112*, 133–137.
36. Baggetto, L.; Jumas, J. C.; Gorka, J.; Bridges, C. A.; Veith, G. M. Predictions of Particle Size and Lattice Diffusion Pathway Requirements for Sodium-Ion Anodes Using $\eta\text{-Cu}_6\text{Sn}_5$ Thin Films as a Model System. *Phys. Chem. Chem. Phys.* **2013**, *15*, 10885–10894.
37. Lin, Y.-M.; Abel, P. R.; Gupta, A.; Goodenough, J. B.; Heller, A.; Mullins, C. B. Sn-Cu Nanocomposite Anodes for Rechargeable Sodium-Ion Batteries. *ACS Appl. Mater. Interfaces* **2013**, *5*, 8273–8277.
38. Wu, L.; Hu, X. H.; Qian, J. F.; Pei, F.; Wu, F. Y.; Mao, R. J.; Ai, X. P.; Yang, H. X.; Cao, Y. L. A Sn-SnS-C Nanocomposite as Anode Host Materials for Na-Ion Batteries. *J. Mater. Chem. A* **2013**, *1*, 7181–7184.
39. Darwiche, A.; Marino, C.; Sougrati, M. T.; Fraisse, B.; Stievano, L.; Monconduit, L. Better Cycling Performances of Bulk Sb in Na-Ion Batteries Compared to Li-Ion Systems: An Unexpected Electrochemical Mechanism. *J. Am. Chem. Soc.* **2012**, *134*, 20805–20811.
40. Qian, J. F.; Chen, Y.; Wu, L.; Cao, Y. L.; Ai, X. P.; Yang, H. X. High Capacity Na-Storage and Superior Cyclability of Nanocomposite Sb/C Anode for Na-Ion Batteries. *Chem. Commun.* **2012**, *48*, 7070–7072.
41. Zhu, Y. J.; Han, X. G.; Xu, Y. H.; Liu, Y. H.; Zheng, S. Y.; Xu, K.; Hu, L. B.; Wang, C. S. Electrospun Sb/C Fibers for a Stable and Fast Sodium-Ion Battery Anode. *ACS Nano* **2013**, *7*, 6378–6386.
42. Nam, D.-H.; Hong, K.-S.; Lim, S.-J.; Kwon, H.-S. Electrochemical Synthesis of a Three-Dimensional Porous Sb/Cu₂Sb Anode for Na-Ion Batteries. *J. Power Sources* **2014**, *247*, 423–427.
43. Baggetto, L.; Ganesh, P.; Sun, C. N.; Meisner, R. A.; Zawodzinski, T. A.; Veith, G. M. Intrinsic Thermodynamic and Kinetic Properties of Sb Electrodes for Li-Ion and Na-Ion Batteries: Experiment and Theory. *J. Mater. Chem. A* **2013**, *1*, 7985–7994.
44. Baggetto, L.; Allcorn, E.; Manthiram, A.; Veith, G. M. Cu₂Sb Thin Films as Anode for Na-Ion Batteries. *Electrochem. Commun.* **2013**, *27*, 168–171.
45. Baggetto, L.; Marszewski, M.; Gorka, J.; Jaroniec, M.; Veith, G. M. AlSb Thin Films as Negative Electrodes for Li-Ion and Na-Ion Batteries. *J. Power Sources* **2013**, *243*, 699–705.
46. Baggetto, L.; Allcorn, E.; Unocic, R. R.; Manthiram, A.; Veith, G. M. Mo₃Sb₇ as a Very Fast Anode Material for Lithium-Ion and Sodium-Ion Batteries. *J. Mater. Chem. A* **2013**, *1*, 11163–11169.

47. Zhou, X.; Dai, Z.; Bao, J.; Guo, Y. G. Wet Milled Synthesis of an Sb/MWCNT Nanocomposite for Improved Sodium Storage. *J. Mater. Chem. A* **2013**, *1*, 13727–13731.
48. Abel, P. R.; Lin, Y.-M.; de Souza, T.; Chou, C.-Y.; Gupta, A.; Goodenough, J. B.; Hwang, G. S.; Heller, A.; Mullins, C. B. Nanocolumnar Germanium Thin Films as a High-Rate Sodium-Ion Battery Anode Material. *J. Phys. Chem. C* **2013**, *117*, 18885–18890.
49. Baggetto, L.; Keum, J. K.; Browning, J. F.; Veith, G. M. Germanium as Negative Electrode Material for Sodium-Ion Batteries. *Electrochem. Commun.* **2013**, *34*, 41–44.
50. Zhang, L.; Holt, C. M. B.; Lubner, E.; Olsen, B. C.; Wang, H.; Danaie, M.; Cui, X.; Tan, X.; Lui, V.; Kalisvaart, W. P.; Mitlin, D. High Rate Electrochemical Capacitors from Three-Dimensional Arrays of Vanadium Nitride-Functionalized Carbon Nanotubes. *J. Phys. Chem. C* **2011**, *115*, 24381–24393.
51. Nimisha, C. S.; Venkatesh, G.; Rao, K. Y.; Rao, G. M.; Munichandraiah, N. Morphology Dependent Electrochemical Performance of Sputter Deposited Sn Thin Films. *Mater. Res. Bull.* **2012**, *47*, 1950–1953.
52. Dichi, E.; Wojakowska, A.; Legendre, B. Study of the Ternary System Germanium-Antimony-Tin: Experimental Phase Diagram. *J. Alloys Compd.* **2001**, *320*, 218–223.
53. Kim, B. G.; Bae, J.; Jeong, S.; Choi, S.; Lee, H. Crystallization Properties of $\text{Ge}_{1-x}\text{Sb}_x$ Thin Films ($x=0.58-0.88$). *Jpn. J. Appl. Phys.* **2011**, *50*, 045805.
54. Chizmeshya, A. V. G.; Bauer, M. R.; Kouvetakis, J. Experimental and Theoretical Study of Deviations from Vegard's Law in the $\text{Sn}_x\text{Ge}_{1-x}$ System. *Chem. Mater.* **2003**, *15*, 2511–2519.
55. Rao, F.; Song, Z. T.; Ren, K.; Li, X. L.; Wu, L. C.; Xi, W.; Liu, B. $\text{Sn}_{12}\text{Sb}_{88}$ Material For Phase Change Memory. *Appl. Phys. Lett.* **2009**, *95*, 032105.
56. Liu, Y. H.; Xu, Y. H.; Zhu, Y. J.; Culver, J. N.; Lundgren, C. A.; Xu, K.; Wang, C. S. Tin-Coated Viral Nanoforests as Sodium-Ion Battery Anodes. *ACS Nano* **2013**, *7*, 3627–3634.
57. Wang, J. W.; Liu, X. H.; Mao, S. X.; Huang, J. Y. Microstructural Evolution of Tin Nanoparticles During in Situ Sodium Insertion and Extraction. *Nano Lett.* **2012**, *12*, 5897–5902.
58. Wong, S. S.; He, G.; Nikzad, S.; Ahn, C. C.; Atwater, H. A. Local Order Measurement in SnGe Alloys and Monolayer Sn Films on Si with Reflection Electron Energy Loss Spectrometry. *J. Vac. Sci. Technol. A* **1995**, *13*, 216–220.
59. Wang, Z. Y.; Wang, Z. C.; Wu, H. B.; Lou, X. W. Mesoporous Single-Crystal $\text{CoSn}(\text{OH})_6$ Hollow Structures with Multi-level Interiors. *Sci. Rep.* **2013**, *3*, 8.
60. Liu, J.; Qiao, S. Z.; Chen, J. S.; Lou, X. W.; Xing, X. R.; Lu, G. Q. Yolk/Shell Nanoparticles: New Platforms for Nanoreactors, Drug Delivery and Lithium-Ion Batteries. *Chem. Commun.* **2011**, *47*, 12578–12591.
61. Song, H. W.; Li, N.; Cui, H.; Wen, X.; Wei, X. L.; Wang, C. X. Significantly Improved High-Rate Li-Ion Batteries Anode by Encapsulating Tin Dioxide Nanocrystals into Mesotunnels. *CrystEngComm* **2013**, *15*, 8537–8543.
62. Hong, Y. J.; Son, M. Y.; Kang, Y. C. One-Pot Facile Synthesis of Double-Shelled SnO_2 Yolk-Shell-Structured Powders by Continuous Process as Anode Materials for Li-ion Batteries. *Adv. Mater.* **2013**, *25*, 2279–2283.
63. Ni, W.; Wang, Y. B.; Xu, R. Formation of $\text{Sn}@C$ Yolk-Shell Nanospheres and Core-Sheath Nanowires for Highly Reversible Lithium Storage. *Part. Part. Syst. Charact.* **2013**, *30*, 873–880.
64. Li, J. P.; Wu, P.; Ye, Y.; Wang, H.; Zhou, Y. M.; Tang, Y. W.; Lu, T. H. Designed Synthesis of $\text{SnO}_2@C$ Yolk-Shell Spheres for High-Performance Lithium Storage. *CrystEngComm* **2014**, *16*, 517–521.
65. Wagemaker, M.; Borghols, W. J. H.; Mulder, F. M. Large Impact of Particle Size on Insertion Reactions. A Case for Anatase Li_xTiO_2 . *J. Am. Chem. Soc.* **2007**, *129*, 4323–4327.
66. Ichitsubo, T.; Doi, T.; Tokuda, K.; Matsubara, E.; Kida, T.; Kawaguchi, T.; Yagi, S.; Okada, S.; Amaki, J.-I. What Determines the Critical Size for Phase Separation in LiFePO_4 in Lithium Ion Batteries? *J. Mater. Chem. A* **2013**, *1*, 14532–14537.
67. Ma, Z.; Li, T.; Huang, Y. L.; Liu, J.; Zhou, Y.; Xue, D. Critical Silicon-Anode Size for Averting Lithiation-Induced Mechanical Failure of Lithium-Ion Batteries. *RSC Adv.* **2013**, *3*, 7398–7402.
68. Vermeulen, P.; Ledovskikh, A.; Danilov, D.; Notten, P. H. L. The Impact of the Layer Thickness on the Thermodynamic Properties of Pd Hydride Thin Film Electrodes. *J. Phys. Chem. B* **2006**, *110*, 20350–20353.
69. Porter, D. A.; Easterling, K. E.; Sherif, M. Y. *Phase Transformations in Metals and Alloys*, 3rd ed. (Revised Reprint); CRC Press, 2009.
70. Tan, X. H.; Harrower, C. T.; Amirkhiz, B. S.; Mitlin, D. Nano-Scale Bi-Layer Pd/Ta, Pd/Nb, Pd/Ti and Pd/Fe Catalysts for Hydrogen Sorption in Magnesium Thin Films. *Int. J. Hydrogen Energy* **2009**, *34*, 7741–7748.
71. Zahiri, B.; Harrower, C. T.; Shalchi Amirkhiz, B.; Mitlin, D. Rapid and Reversible Hydrogen Sorption in Mg-Fe-Ti Thin Films. *Appl. Phys. Lett.* **2009**, *95*, 103114–103114–3.
72. Zahiri, B.; Amirkhiz, B. S.; Mitlin, D. Hydrogen Storage Cycling of MgH_2 Thin Film Nanocomposites Catalyzed by Bimetallic Cr-Ti. *Appl. Phys. Lett.* **2010**, *97*, 083106–083106–3.
73. Mortazavi, M.; Deng, J. K.; Shenoy, V. B.; Medhekar, N. V. Elastic Softening of Alloy Negative Electrodes for Na-Ion Batteries. *J. Power Sources* **2013**, *225*, 207–214.
74. Stournara, M. E.; Xiao, X.; Qi, Y.; Johari, P.; Lu, P.; Sheldon, B. W.; Gao, H.; Shenoy, V. B. Li Segregation Induces Structure and Strength Changes at the Amorphous Si/Cu Interface. *Nano Lett.* **2013**, *13*, 4759–4768.
75. Datta, M. K.; Epur, R.; Saha, P.; Kadakia, K.; Park, S. K.; Kumta, P. N. Tin and Graphite Based Nanocomposites: Potential Anode For Sodium Ion Batteries. *J. Power Sources* **2013**, *225*, 316–322.
76. Karki, K.; Zhu, Y.; Liu, Y.; Sun, C.-F.; Hu, L.; Wang, Y.; Wang, C.; Cumings, J. Hoop-Strong Nanotubes for Battery Electrodes. *ACS Nano* **2013**, *7*, 8295–8302.
77. Song, T.; Cheng, H.; Choi, H.; Lee, J.-H.; Han, H.; Hyun Lee, D.; Su Yoo, D.; Kwon, M.-S.; Choi, J.-M.; Gwang Doo, S.; Chang, H.; Xiao, J.; Huang, Y.; Park, W. I.; Chung, Y.-C.; Kim, H.; Rogers, J. A.; Paik, U. Si/Ge Double-Layered Nanotube Array as a Lithium Ion Battery Anode. *ACS Nano* **2012**, *6*, 303–309.
78. Liu, N.; Wu, H.; McDowell, M. T.; Yao, Y.; Wang, C.; Cui, Y. A Yolk-Shell Design for Stabilized and Scalable Li-Ion Battery Alloy Anodes. *Nano Lett.* **2012**, *12*, 3315–3321.
79. Yao, Y.; McDowell, M. T.; Ryu, I.; Wu, H.; Liu, N. A.; Hu, L. B.; Nix, W. D.; Choi, J. W.; Cui, Y. Interconnected Silicon Hollow Nanospheres for Lithium-Ion Battery Anodes with Long Cycle Life. *Nano Lett.* **2011**, *11*, 2949–2954.
80. Memarzadeh, E.; Kalisvaart, W. P.; Cui, K.; Kohandehghan, A.; Kupsta, M.; Olsen, B. C.; Mitlin, D. ALD TiO_2 Coated Silicon Nanowires for Lithium Ion Battery Anodes with Enhanced Cycling Stability and Coulombic Efficiency. *Phys. Chem. Chem. Phys.* **2013**, *15*, 13646–13657.
81. Kohandehghan, A.; Kalisvaart, W. P.; Cui, K.; Kupsta, M.; Memarzadeh, E.; Mitlin, D. Silicon Nanowire Lithium-Ion Battery Anodes with ALD Deposited TiN Coatings Demonstrate a Major Improvement in Cycling Performance. *J. Mater. Chem. A* **2013**, *1*, 12850–12861.
82. McDowell, M. T.; Lee, S. W.; Ryu, I.; Wu, H.; Nix, W. D.; Choi, J. W.; Cui, Y. Novel Size and Surface Oxide Effects in Silicon Nanowires as Lithium Battery Anodes. *Nano Lett.* **2011**, *11*, 4018–4025.
83. Aurbach, D.; Markovsky, B.; Levi, M. D.; Levi, E.; Schechter, A.; Moshkovich, M.; Cohen, Y. New Insights into the Interactions Between Electrode Materials and Electrolyte Solutions for Advanced Nonaqueous Batteries. *J. Power Sources* **1999**, *81*, 95–111.
84. Aurbach, D. Review of Selected Electrode-Solution Interactions which Determine the Performance of Li and Li Ion Batteries. *J. Power Sources* **2000**, *89*, 206–218.
85. Levi, M. D.; Aurbach, D. Simultaneous Measurements and Modeling of the Electrochemical Impedance and the

- Cyclic Voltammetric Characteristics of Graphite Electrodes Doped with Lithium. *J. Phys. Chem. B* **1997**, *101*, 4630–4640.
86. Kohandehghan, A.; Kalisvaart, P.; Kupsta, M.; Zahiri, B.; Amirkhiz, B. S.; Li, Z. P.; Memarzadeh, E. L.; Bendersky, L. A.; Mitlin, D. Magnesium and Magnesium-Silicide Coated Silicon Nanowire Composite Anodes for Lithium-Ion Batteries. *J. Mater. Chem. A* **2013**, *1*, 1600–1612.
 87. Etacheri, V.; Geiger, U.; Gofer, Y.; Roberts, G. A.; Stefan, I. C.; Fasching, R.; Aurbach, D. Exceptional Electrochemical Performance of Si-Nanowires in 1,3-Dioxolane Solutions: A Surface Chemical Investigation. *Langmuir* **2012**, *28*, 6175–6184.
 88. Oh, S. M.; Myung, S. T.; Jang, M. W.; Scrosati, B.; Hassoun, J.; Sun, Y. K. An Advanced Sodium-Ion Rechargeable Battery Based on a Tin-Carbon Anode and a Layered Oxide Framework Cathode. *Phys. Chem. Chem. Phys.* **2013**, *15*, 3827–3833.
 89. Nakai, H.; Kubota, T.; Kita, A.; Kawashima, A. Investigation of the Solid Electrolyte Interphase Formed by Fluoroethylene Carbonate on Si Electrodes. *J. Electrochem. Soc.* **2011**, *158*, A798–A801.
 90. Etacheri, V.; Haik, O.; Goffer, Y.; Roberts, G. A.; Stefan, I. C.; Fasching, R.; Aurbach, D. Effect of Fluoroethylene Carbonate (FEC) on the Performance and Surface Chemistry of Si-Nanowire Li-Ion Battery Anodes. *Langmuir* **2012**, *28*, 965–976.
 91. Han, X.; Liu, Y.; Jia, Z.; Chen, Y.-C.; Wan, J.; Weadock, N.; Gaskell, K. J.; Li, T.; Hu, L. Atomic-Layer-Deposition Oxide Nano-Glue for Sodium Ion Batteries. *Nano Lett.* **2014**, *14*, 139–147.
 92. Wang, Y.; Su, D. W.; Wang, C. Y.; Wang, G. X. SnO₂@MWCNT Nanocomposite as a High Capacity Anode Material for Sodium-Ion Batteries. *Electrochem. Commun.* **2013**, *29*, 8–11.
 93. Sun, Q.; Ren, Q. Q.; Li, H.; Fu, Z. W. High Capacity Sb₂O₄ Thin Film Electrodes for Rechargeable Sodium Battery. *Electrochem. Commun.* **2011**, *13*, 1462–1464.
 94. Wang, Y.-X.; Lim, Y.-G.; Park, M.-S.; Chou, S.-L.; Kim, J. H.; Liu, H.-K.; Dou, S.-X.; Kim, Y.-J. Ultrafine SnO₂ Nanoparticle Loading onto Reduced Graphene Oxide as Anodes for Sodium-Ion Batteries with Superior Rate and Cycling Performances. *J. Mater. Chem. A* **2014**, *2*, 529–534.
 95. Wu, L.; Hu, X. H.; Qian, J. F.; Pei, F.; Wu, F. Y.; Mao, R. J.; Ai, X. P.; Yang, H. X.; Cao, Y. L. Sb-C Nanofibers with Long Cycle Life as an Anode Material for High-Performance Sodium-Ion Batteries. *Energ. Environ. Sci.* **2014**, *7*, 323–328.
 96. Han, X. G.; Liu, Y.; Jia, Z.; Chen, Y. C.; Wan, J. Y.; Weadock, N.; Gaskell, K. J.; Li, T.; Hu, L. B. Atomic-Layer-Deposition Oxide Nanoglue for Sodium Ion Batteries. *Nano Lett.* **2014**, *14*, 139–147.
 97. Boolchand, P.; Koch, C. C. Moessbauer Spectroscopy Study of Nanoscale Ge-Sn Dispersions Prepared by Ball Milling. *J. Mater. Res.* **1992**, *7*, 2876–2883.
 98. Rebelo, Q. H. F.; Cotta, E. A.; de Souza, S. M.; Trichês, D. M.; Machado, K. D.; de Lima, J. C.; Grandi, T. A.; Poffo, C. M.; Manzato, L. Structural and Vibrational Investigations on Ge₃₄Sb₆₆ Solid Solutions Produced by Mechanical Alloying. *J. Alloys Compd.* **2013**, *575*, 80–85.
 99. Tan, L. P.; Sun, T.; Fan, S.; Ramanujan, R. V.; Hng, H. H. Facile Precipitation of Two Phase Alloys in SnTe_{0.75}Se_{0.25} with Improved Power Factor. *J. Alloys Compd.* **2014**, *587*, 420–427.
 100. Fan, S. F.; Lim, L. Y.; Tay, Y. Y.; Pramana, S. S.; Rui, X. H.; Samani, M. K.; Yan, Q. Y.; Tay, B. K.; Toney, M. F.; Hng, H. H. Rapid Fabrication of a Novel Sn-Ge Alloy: Structure-Property Relationship and Its Enhanced Lithium Storage Properties. *J. Mater. Chem. A* **2013**, *1*, 14577–14585.